The Astrophysical Journal Letters, 983:L40 (21pp), 2025 April 20 https://doi.org/10.3847/2041-8213/adc1c8

New Constraints on DMS and DMDS in the Atmosphere of K2-18 b from JWST MIRI

Nikku Madhusudhan[1], Savvas Constantinou[1,6], Måns Holmberg[2,6], Subhajit Sarkar[3,6], Anjali A. A. Piette[4], and Julianne I. Moses[5]

[1] Institute of Astronomy, University of Cambridge, Madingley Road, Cambridge, CB3 0HA, UK; nmadhu@ast.cam.ac.uk
[2] Space Telescope Science Institute, 3700 San Martin Drive, Baltimore, MD 21218, USA
[3] School of Physics and Astronomy, Cardiff University, The Parade, Cardiff, CF24 3AA, UK
[4] School of Physics and Astronomy, University of Birmingham, Edgbaston, Birmingham, B15 2TT, UK
[5] Space Science Institute, Boulder, CO 80301, USA

Received 2024 December 13; revised 2025 March 14; accepted 2025 March 15; published 2025 April 17

Abstract

The sub-Neptune frontier has opened a new window into the rich diversity of planetary environments beyond the solar system. The possibility of hycean worlds, with planet-wide oceans and H_2-rich atmospheres, significantly expands and accelerates the search for habitable environments elsewhere. Recent JWST transmission spectroscopy of the candidate hycean world K2-18 b in the near-infrared led to the first detections of the carbon-bearing molecules CH_4 and CO_2 in its atmosphere, with a composition consistent with predictions for hycean conditions. The observations also provided a tentative hint of dimethyl sulfide (DMS), a possible biosignature gas, but the inference was of low statistical significance. We report a mid-infrared transmission spectrum of K2-18 b obtained using the JWST MIRI LRS instrument in the ~6–12 μm range. The spectrum shows distinct features and is inconsistent with a featureless spectrum at 3.4σ significance compared to our canonical model. We find that the spectrum cannot be explained by most molecules predicted for K2-18 b, with the exception of DMS and dimethyl disulfide (DMDS), also a potential biosignature gas. We report new independent evidence for DMS and/or DMDS in the atmosphere at 3σ significance, with high abundance ($\gtrsim$10 ppmv) of at least one of the two molecules. More observations are needed to increase the robustness of the findings and resolve the degeneracy between DMS and DMDS. The results also highlight the need for additional experimental and theoretical work to determine accurate cross sections of important biosignature gases and identify potential abiotic sources. We discuss the implications of the present findings for the possibility of biological activity on K2-18 b.

Unified Astronomy Thesaurus concepts: Exoplanets (498); Biosignatures (2018); Habitable planets (695)

1. Introduction

The discoveries of temperate exoplanets orbiting nearby stars and the advent of the James Webb Space Telescope (JWST; J. P. Gardner et al. 2006) are opening up the possibility of detecting biosignatures on habitable exoplanets. While habitable exoplanets orbiting Sun-like stars are still beyond the reach of JWST, such planets orbiting smaller M dwarf stars are within the range of observability with JWST. A number of low-mass exoplanets orbiting M dwarfs have been observed in recent years, highlighting their diversity and both the challenges of and opportunities in characterizing their atmospheres with JWST (e.g., O. Lim et al. 2023; N. Madhusudhan et al. 2023b; E. M. May et al. 2023; S. E. Moran et al. 2023; L. Alderson et al. 2024; B. Benneke et al. 2024; M. Damiano et al. 2024; N. Scarsdale et al. 2024; M. Holmberg & N. Madhusudhan 2024; N. L. Wallack et al. 2024; M. K. Alam et al. 2025).

The Hycean paradigm developed in recent years has the potential to significantly expand and accelerate the search for life elsewhere (N. Madhusudhan et al. 2021). Hycean worlds are planets with habitable ocean-covered surfaces and H_2-rich atmospheres. Their lower densities, larger sizes, and lighter atmospheres compared to Earth-like planets make hycean worlds more readily detectable and more conducive for atmospheric characterization. Similarly, their wider habitable zone compared to Earth-like planets also makes them more abundant, with over a dozen hycean candidates already identified (e.g., N. Madhusudhan et al. 2021; A. Fukui et al. 2022; K. Kawauchi et al. 2022; T. Mikal-Evans et al. 2023; C. Piaulet et al. 2023).

Early observations with JWST have bolstered the promise of this new avenue, starting with the candidate hycean world K2-18 b. The planet has a mass of 8.63 ± 1.35 $M_\oplus$ and a radius of 2.61 ± 0.09 $R_\oplus$ (B. Benneke et al. 2019; R. Cloutier et al. 2019), and it orbits in the habitable zone of an M2.5V star (B. T. Montet et al. 2015; R. Cloutier et al. 2017; P. Sarkis et al. 2018). The bulk parameters of the planet are consistent with a degenerate set of internal structures, including a hycean world, a mini-Neptune or a gas dwarf, i.e., a rocky planet with a thick H_2-rich atmosphere (N. Madhusudhan et al. 2020). Atmospheric observations are key to breaking the degeneracy.

A transmission spectrum of K2-18 b obtained with the Hubble Space Telescope WFC3/G141 spectrograph (1.1–1.7 μm) was initially used to infer the presence of water vapor (H_2O) in its atmosphere (B. Benneke et al. 2019; A. Tsiaras et al. 2019; N. Madhusudhan et al. 2020). However, significant degeneracies were found between potential absorption due to H_2O and that due to methane (CH_4; B. Bézard et al. 2022; D. Blain et al. 2021) or contributions from stellar heterogeneities (T. Barclay et al. 2021). Transmission spectroscopy of K2-18 b with JWST led to the first detections of carbon-bearing molecules, CH_4 and carbon dioxide

---

[6] These authors contributed equally to this work; the naming order is alphabetical.

(CO_2), at 5σ and 3σ significance, respectively, in its H_2-rich atmosphere (N. Madhusudhan et al. 2023b). The high sensitivity and wide wavelength range of the JWST spectrum helped resolve the previous CH_4–H_2O degeneracy, resulting in a strong detection of CH_4 and nondetection of H_2O. The nondetection of H_2O was consistent with the low photospheric temperature retrieved, implying H_2O condensation at the altitudes probed by the transmission spectrum (N. Madhusudhan et al. 2023a, 2023b).

The retrieved atmospheric composition of K2-18 b also provided important constraints on its internal structure. The detections of CH_4 and CO_2 at significant abundances, along with the nondetections of ammonia (NH_3) and carbon monoxide (CO) and the overall high CO_2/CO ratio, are consistent with prior predictions for a hycean atmosphere (R. Hu 2021; S.-M. Tsai et al. 2021; N. Madhusudhan et al. 2023a). Other scenarios requiring a deep H_2-rich atmosphere, such as a mini-Neptune or a gas dwarf, as mentioned above, are inconsistent with the retrieved abundances (N. Madhusudhan et al. 2023b). For example, a mini-Neptune scenario (e.g., N. F. Wogan et al. 2024) is incompatible with most of the retrieved abundances, especially the low NH_3 and high CO_2/CO ratio (G. J. Cooke & N. Madhusudhan 2024; C. R. Glein 2024). Similarly, models considering NH_3 depletion due to magma oceans (O. Shorttle et al. 2024) in the gas dwarf scenario were found to be inconsistent with mass and density constraints, among other factors, while also being inconsistent with the retrieved composition (F. E. Rigby et al. 2024). Therefore, presently, the atmospheric abundances of K2-18 b are best explained by a hycean world scenario and are incompatible with mini-Neptune or gas dwarf scenarios requiring a deep H_2-rich atmosphere.

Open questions remain as to the possibility of habitable conditions on K2-18 b. While the atmospheric composition is consistent with predictions for hycean conditions (N. Madhusudhan et al. 2023b) and a large water inventory in the interior (C. N. Luu et al. 2024; J. Yang & R. Hu 2024), the nature of the possible ocean beneath the H_2-rich atmosphere is unknown. A habitable liquid water ocean requires an adequate albedo (A_B) due to clouds/hazes (A. A. A. Piette & N. Madhusudhan 2020; N. Madhusudhan et al. 2021), with the latest theoretical estimate of the required albedo being $A_B > 0.5$–0.6 (J. Leconte et al. 2024), similar to that assumed for candidate hycean worlds (N. Madhusudhan et al. 2021). A cloud-/haze-free atmosphere would render the surface too hot to be habitable and/or have water in a supercritical state (N. Madhusudhan et al. 2020; A. A. A. Piette & N. Madhusudhan 2020; M. Scheucher et al. 2020; H. Innes et al. 2023; R. T. Pierrehumbert 2023; J. Leconte et al. 2024). While the required albedo may be consistent with the evidence for clouds/hazes reported at the day–night terminator of K2-18 b (N. Madhusudhan et al. 2023b), and is within the range of A_B of 0.3–0.8 known for atmospheres of most solar system planets, the dayside albedo of K2-18 b has not been measured directly.

On the other hand, recent studies have also indicated the potential for biotic conditions on K2-18 b. The CH_4 on K2-18 b may be contributed, partly or predominantly, from biogenic sources, similar to CH_4 from methanogenic bacteria on Earth (N. Madhusudhan et al. 2023a, 2023b; G. J. Cooke & N. Madhusudhan 2024; N. F. Wogan et al. 2024). In particular, the detection of abundant CH_4 alongside CO_2 in a shallow H_2-rich atmosphere is more easily explained by an inhabited hycean scenario than an uninhabited case (G. J. Cooke & N. Madhusudhan 2024; N. F. Wogan et al. 2024). The CH_4–CO_2 pair has also been proposed as a promising biosignature for Earth-like habitable exoplanets, as may have been the case for the early Earth (J. Krissansen-Totton et al. 2018). However, the prospect of abiotically produced CH_4 through atmospheric chemistry cannot be ruled out in the uninhabited hycean scenario for K2-18 b (G. J. Cooke & N. Madhusudhan 2024). Another potential indication of biological activity was suggested by a weak ($\lesssim 2\sigma$) inference of dimethyl sulfide (DMS) in K2-18 b with previous JWST observations (N. Madhusudhan et al. 2023b).

The tentative inference of DMS in K2-18 b opens an important debate as to the possible presence of life on K2-18 b. On the one hand, the low detection significance highlights the challenges in detecting such molecules. In the case of the previous JWST observations of K2-18 b, the detection significance of DMS depended on the relative offsets between the spectra observed from different detectors on the JWST NIRISS and NIRSpec instruments, ranging from 2.4σ with no offsets to below 1σ for two offsets (N. Madhusudhan et al. 2023b). Another challenge is the strong degeneracy between the spectral features of DMS near 3.3 μm and 4.3 μm with strong features of CH_4 and CO_2 at overlapping wavelengths, as well as potential contributions from other hydrocarbons with strong features in the 3–5 μm range (N. Madhusudhan et al. 2023b; S.-M. Tsai et al. 2024). On the other hand, a confident detection of a molecule like DMS would serve as a more robust biosignature than molecules like CH_4, which are more easily detectable but may be present in abundance through abiotic chemistry.

The robustness of DMS as a biosignature in H_2-rich environments has been proposed extensively in the literature both for rocky planets (S. D. Domagal-Goldman et al. 2011; S. Seager et al. 2013a; D. C. Catling et al. 2018; E. W. Schwieterman et al. 2018) and hycean worlds (N. Madhusudhan et al. 2021). Despite the low detection significance, the reported abundance constraints of DMS are physically plausible for realistic levels of biogenic sources (N. Madhusudhan et al. 2023b; S.-M. Tsai et al. 2024). In particular, DMS mixing ratios as high as 10^{-2} are possible in K2-18 b for high biogenic fluxes of sulfur-based biosignature gases above ~20 times Earth levels (S.-M. Tsai et al. 2024).

In this work, we conduct an independent search for molecular species, including DMS, in K2-18 b in a different wavelength range, using the JWST MIRI spectrograph. As discussed above, the previous tentative inference of DMS in K2-18 b was made using a near-infrared transmission spectrum in the 1–5 μm range obtained with the JWST NIRISS and NIRSpec instruments. However, the evidence for DMS was affected by potential flux offsets between the different detectors (N. Madhusudhan et al. 2023b). Therefore, an independent search for DMS and other such molecules using a different instrument in a complementary spectral range is invaluable for assessing the significance of prior findings and for providing an independent line of evidence. Mid-infrared spectroscopy with JWST provides a promising avenue in this direction. In addition to providing a complementary spectral window (~5–12 μm) to previous observations, this wavelength range also encompasses strong spectral features of DMS and several other biosignature gases (S. D. Domagal-Goldman et al. 2011; S. Seager et al. 2013b; E. W. Schwieterman et al. 2018; S.-M. Tsai et al. 2024).

We present a mid-infrared transmission spectrum of K2-18 b with JWST, the first for a habitable-zone exoplanet. This allows for an independent search for DMS and other biosignature gases in the atmosphere of K2-18 b, as discussed above. In what follows, we present our observations, data reduction, and light-curve analyses in Section 2. We discuss our retrieval approach and present the atmospheric inferences obtained from the transmission spectrum in Section 3. We summarize our results and discuss the implications in Section 4.

2. Observations and Data Reduction

We report a mid-infrared transmission spectrum of K2-18 b using the JWST MIRI low-resolution spectrograph (LRS; S. Kendrew et al. 2015; J. Bouwman et al. 2023). The observations were conducted as part of JWST GO Program 2722 (PI: N. Madhusudhan). The observations were made in the slitless prism configuration with the F560W filter and the FASTR1 readout pattern. The target acquisition was conducted on the science target, the host star K2-18, which is an M2.5V dwarf star with J mag of 9.763 (R. Cloutier et al. 2017). The science exposure was performed between 23:13:29 UTC on 2024 April 25 and 05:04:37 UTC on 2024 April 26, for a duration of 5.85 hr, with an in-transit duration of 2.68 hr and the remaining time providing the out-of-transit baseline. The science observation consists of a total of 5095 integrations, with 25 groups per integration. The maximum fraction of saturation across the detector was calculated to be 51%, using the JWST Exposure Time Calculator. The spectrum spans a wavelength range of $\sim$5–12 μm with an average native resolution of $R \sim 100$. No high-gain antenna movement was reported during the observations. We carry out the data reduction and light-curve analysis in two parallel efforts, using independent pipelines and sensitivity analyses, as described below.

2.1. JExoRES Pipeline

We employ a modified version of the `JExoRES` pipeline (M. Holmberg & N. Madhusudhan 2023; N. Madhusudhan et al. 2023b), adapted to MIRI LRS. First, we perform Stages 1–2, using the JWST Science Calibration Pipeline (H. Bushouse 2020) to perform calibrations and the detector ramp fitting. In Stage 1, we perform the data quality initialization, electromagnetic interference (EMI) correction, saturation flagging, first and last frame flagging, linearity correction, reset switch charge decay (RSCD) correction, dark-current subtraction, and ramp fitting. For this, we use both the standard linearity and RSCD corrections and a custom approach detailed in Appendix A.2, as pursued by several recent works (D. Grant et al. 2023; E. M. R. Kempton et al. 2023; A. Dyrek et al. 2024). Overall, we find that the approach to nonlinearity correction has a minimal effect on the transmission spectrum of K2-18 b, as discussed in Appendix A.2 and illustrated in Figure 7. Next, we perform the flat-field correction in Stage 2.

In Stage 3, we first use the gain reference file to convert the flux from DN s^{-1} to e^{-} s^{-1}. We then search for cosmic-ray hits by performing sigma clipping on the time series of each pixel by first removing a running median of seven integrations and using a threshold of 7σ. In addition, we also mask neighboring pixels surrounding detected outliers as well as pixels that have been flagged with any issues during Stages 1–2. We then correct for the background by subtracting the mean of the flux outside the trace, for each detector column and integration. To estimate the background, we use columns with pixel numbers 11–30 and 44–63, while not including bad pixels or outliers.

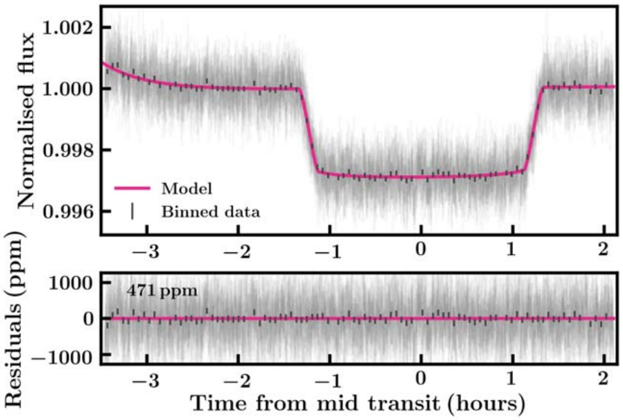

Figure 1. MIRI LRS white-light curve of K2-18 b. The light curve is based on the time-series spectroscopic data binned between 4.8 and 10 μm, discarding the first 250 integrations. The top panel shows the white-light curve with and without binning, together with the median model fit. The lower panel shows the residuals after subtracting the model. The standard deviation of the residuals without binning is 471 ppm—corresponding to 1.25 times the expected noise level from photon noise and read noise.

Finally, we extract the spectra with optimal extraction (K. Horne 1986), using the median of all integrations as a model for the point-spread function for each spectral channel. For this, we use an aperture of 9 pixels. A box extraction approach produces very similar results, as shown in Figure 8. We reject additional outliers during optimal extraction and then in the light curves themselves, using sigma clipping with a running median filter.

Next, we fit the light curves using the `batman` (L. Kreidberg 2015) transit model and perform nested sampling with `MultiNest` (F. Feroz et al. 2009), assuming a circular orbit with a period from B. Benneke et al. (2019). We first construct a white-light curve by integrating the flux between 4.8 and 10 μm. Using this wavelength range gave slightly lower (5%) scatter compared to the full 4.8–12 μm range. For fitting the light curve, we use normally distributed priors on the normalized semimajor axis a/R_* and the inclination i from the weighted average of the NIRISS and NIRSpec fits from N. Madhusudhan et al. (2023b). These orbital parameters are also consistent with pre-JWST measurements (B. Benneke et al. 2019; A. Tsiaras et al. 2019). For the limb darkening, we use the quadratic law with the parameterization and priors by D. M. Kipping (2013). We use wide uniform priors on all other parameters. For the baseline trend, we adopt an exponential and a linear component: $F_{\rm obs}(t) = F_{\rm out}\,(1 + \alpha\tau + \gamma e^{-\tau/\epsilon})\,F_{\rm transit}(t)$, where τ is the time since the start of the observation, $F_{\rm transit}$ is the `batman` transit model, and $F_{\rm out}$, α, γ, and ϵ are trend parameters. Furthermore, we mask the first 250 integrations (1034 s) to remove the strongest effect of the detector settling. Figure 1 shows the MIRI white-light curve of K2-18 b together with our model fit. Moreover, we also fit for an error inflation parameter to account for additional white noise. The parameters measured from the white-light-curve fitting are shown in Table 1.

Finally, we perform the spectroscopic light-curve fitting, fixing a/R_*, i, the mid-transit time, and the two limb-darkening coefficients to the values obtained from the white-light curve. We bin the light curves in wavelength prior to fitting, nominally with a width of 0.2 μm or 5 pixels, whichever contains the most pixels, as described in Appendix A.4. A

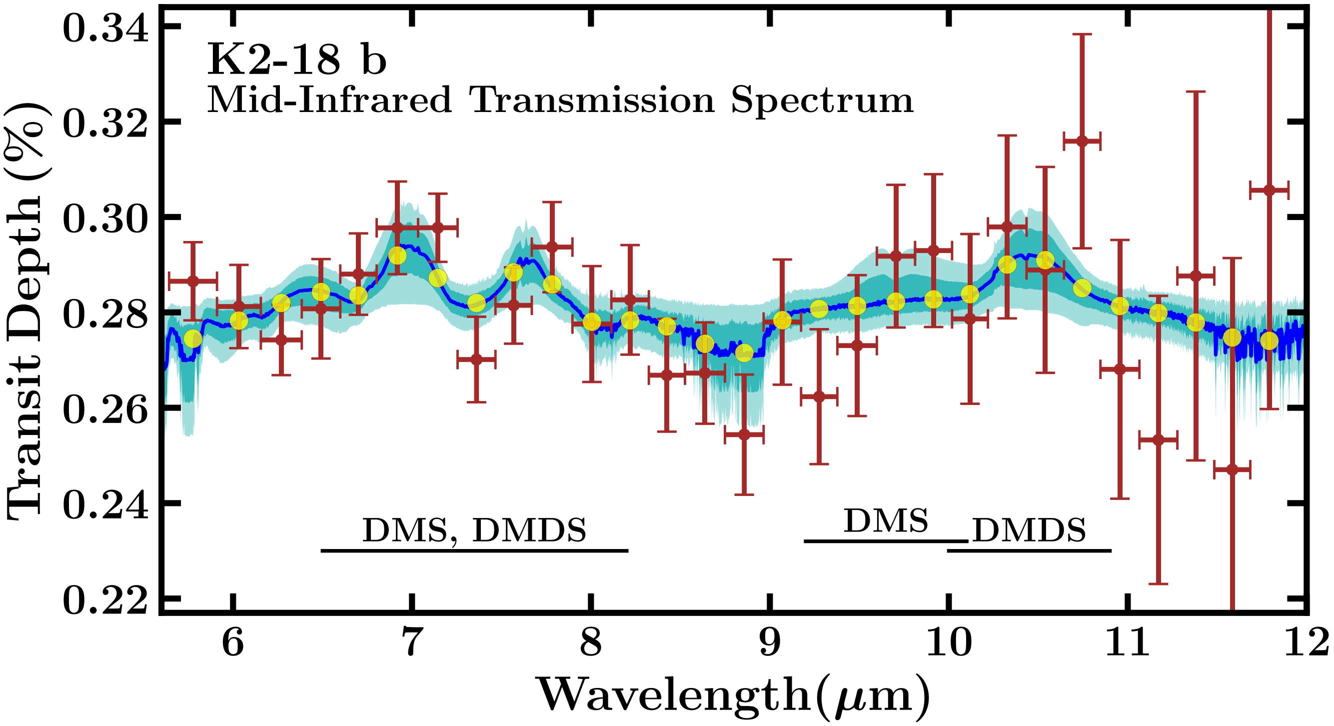

Figure 2. The mid-infrared transmission spectrum of K2-18 b obtained with the JWST MIRI LRS instrument. The data points with error bars (in brown) show the observed spectrum as described in Section 2.1. The horizontal error bars correspond to the spectral bin width. The dark blue curve denotes the median retrieved spectral fit, while the two lighter shaded regions denote the 1σ and 2σ intervals. The prominent features of DMS and DMDS are identified. Both molecules have overlapping spectral features between 6.8 and 8 μm, with broader features between ∼9 and 10 μm for DMS and ∼10–11 μm for DMDS. The individual spectral contributions of these molecules are shown in Figure 4.

Table 1
Parameters Estimated from the White-light-curve Analysis of Our JWST MIRI LRS Observation of K2-18 b

Parameter	`JExoRES`	`JexoPipe`
Mid-transit time, T_0 (BJD – 2400000.5)	$60426.128786^{+0.000082}_{-0.000082}$	$60426.128853^{+0.000081}_{-0.000080}$
Inclination, i (deg)	$89.5598^{+0.0068}_{-0.0066}$	$89.5600^{+0.0067}_{-0.0067}$
Normalized semimajor axis, a/R_*	$80.34^{+0.47}_{-0.45}$	$80.39^{+0.46}_{-0.47}$
Planet-to-star radius ratio, R_p/R_*	$0.05332^{+0.00017}_{-0.00018}$	$0.05352^{+0.00018}_{-0.00019}$
First limb-darkening coefficient, u_1	$0.037^{+0.056}_{-0.028}$	$0.033^{+0.046}_{-0.024}$
Second limb-darkening coefficient, u_2	$0.114^{+0.047}_{-0.105}$	$0.071^{+0.046}_{-0.058}$

Note. The results are shown from the two independent data analyses. In both cases, the period was fixed to 32.940045 days (B. Benneke et al. 2019) and wavelengths between 4.8 and 10 μm were used.

minimum bin width of 0.2 μm is in line with the bin widths used in previous works, ranging between 0.15 and 0.5 μm (e.g., J. Bouwman et al. 2023; D. Grant et al. 2023; T. J. Bell et al. 2024; D. Powell et al. 2024). Due to instability of the spectrum below 5.6 μm as a function of binning, we disregard this part from further analysis, to be conservative, as discussed in Appendix A.4. We again mask the first 250 integrations. We explore different choices of trends in Appendix A.5 and find that an exponential and a linear component produce a stable transmission spectrum when varying the number of integrations to mask at the start. Furthermore, we find evidence for time-correlated noise on the timescale of minutes, with increasing amplitude toward shorter wavelengths. Accounting for this additional noise using Gaussian processes (GPs), as described in Appendix A.7, we find that the transit depth uncertainty increases by around 30% at 6 μm, and less at longer wavelengths. We also test different assumptions for the limb darkening and find that it does not significantly alter the transmission spectrum, as shown in Appendix A.6. The resulting MIRI transmission spectrum of K2-18 b is shown in Figure 2.

2.2. *JexoPipe Pipeline*

We use a second pipeline, `JexoPipe`, a JWST data reduction framework previously applied to NIRSpec Prism and G395H data (S. Sarkar et al. 2024) and adapted here for MIRI LRS. Starting with the .uncal files, in Stage 1 we utilize the official JWST Science Calibration Pipeline steps in the following sequence: group scale, data quality array initialization, EMI correction, saturation flagging, first frame, last frame, reset, linearity correction, RSCD correction, dark subtraction, jump detection, ramp fitting, and gain scale. Stage 1 ends with integration-level .rateints files. After combining all Stage 1 segments into a single .rateints file, we begin Stage 2 by applying the JWST calibration pipeline steps: assign World Coordinate System (WCS) and flat field. We then apply a

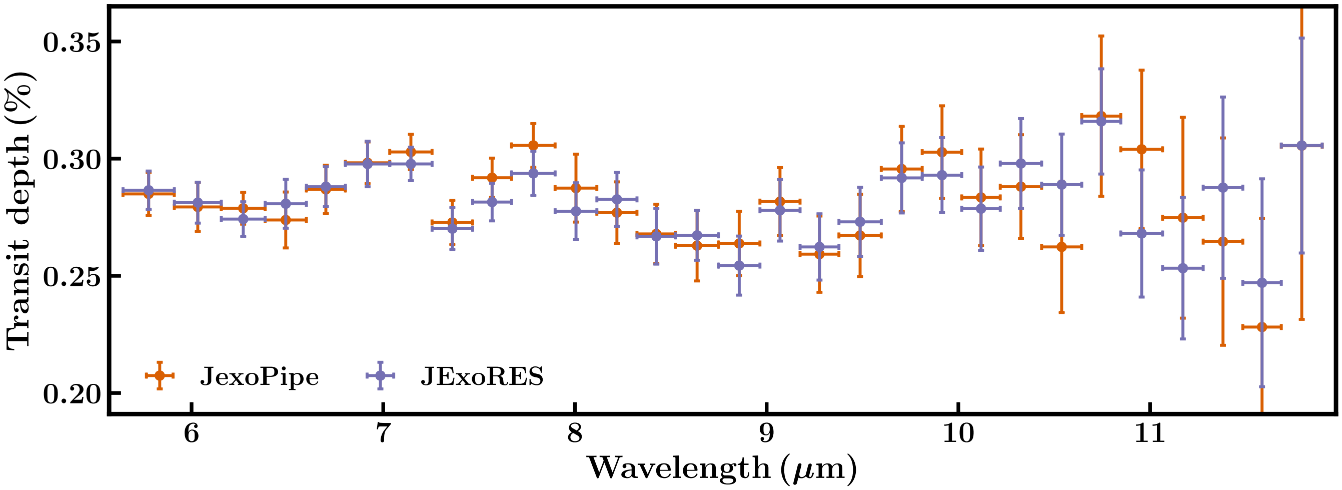

Figure 3. Demonstration of the stability of the MIRI transmission spectrum of K2-18 b using two independent data reduction pipelines. The spectra from the `JExoRES` and `JexoPipe` pipelines are shown in purple and orange, respectively, and are further described in Sections 2.1 and 2.2.

custom bad-pixel flagging step (S. Sarkar et al. 2024). This step applies NaN values to all pixels that have abnormal Data Quality (DQ) flags as well as to 3σ outliers found on a row-by-row basis in each integration image. Next, we perform background subtraction per integration, using pixel columns (10)–(14) and (60)–(66). We apply an outlier mask, then subtract the mean of each row from all pixel values in that row.

We then apply a custom bad-pixel correction step using a combination of temporal and spatial interpolation, as described in S. Sarkar et al. (2024). Next, we detect the remaining outliers for each integration by comparison with a rolling median (of 20 contiguous integrations), replacing pixel values $\pm 5\sigma$ from the rolling median with the median value. For Stage 3, 1D spectral extraction, for each integration, we apply an aperture of 9 pixel columns centered on the spectrum maximum and then perform optimal extraction (K. Horne 1986). We obtain the wavelength for each pixel row from the mean of the wavelengths in that row after application of the aperture.

We use the 1D spectra time series to construct a white-light curve (between 4.8 and 10 μm). We exclude the first 250 integrations, where the systematic trend is most extreme. We identify outliers on the white-light curve, $\pm 2.5\sigma$ from a rolling median, and replace the 1D spectra corresponding to these outliers with linearly interpolated spectra from adjacent integrations. We scale the error bars on the light-curve points such that the average error bar equals the observed standard deviation of the scatter in the out-of-transit residuals. We use `emcee` (D. Foreman-Mackey et al. 2013) to perform a Markov Chain Monte Carlo parameter estimation of the white-light curve, fitting for a transit model with quadratic limb darkening generated by `pylightcurve` (A. Tsiaras et al. 2016) multiplied by a systematic trend consisting of an exponential term and a linear term (as in Section 2.1). In the white-light curve, we fit for R_p/R_*, the mid-transit time, a/R_*, i, quadratic limb-darkening coefficients, and four parameters for the trend. Uniform priors are used except for a/R_* and i, where we apply Gaussian priors based on values in N. Madhusudhan et al. (2023b) and use the Kipping parameterization (D. M. Kipping 2013) for limb-darkening priors. We fix the period to 32.940045 days (B. Benneke et al. 2019), the argument of periastron to 90°, and the eccentricity to 0. The white-light-curve parameter estimates are given in Table 1.

We bin the spectral light curves following the same prescription as in Section 2.1. We fit the spectral light curves in a similar manner to the white-light curve, with the exception of the mid-transit time, a/R_*, and i, which we fix to the white-light values. We also fix the limb-darkening coefficients to those from the white-light fit. To check the sensitivity of the transmission spectrum to the treatment of limb darkening, we also adopt fixed wavelength-dependent limb-darkening coefficients from ExoTic-LD (the Kurucz model; D. Grant & H. R. Wakeford 2024). In doing so, we find that the spectra from the two treatments are consistent to well within the 1σ uncertainties.

For each spectral light-curve fit, the free parameters are R_p/R_* and the four systematic trend parameters. To account for time-correlated noise, we obtain the β factor for each spectral light curve, using the "time-averaging" method to produce Allan deviation plots (J. N. Winn et al. 2007; P. Cubillos et al. 2017). The spectral light-curve fits are then rerun after inflating the uncertainties on the original light curves by the corresponding β value. The final transmission spectrum is shown in Figure 3.

2.3. Robustness of the Transmission Spectrum

The transmission spectra obtained from the two pipelines show good agreement, as shown in Figure 3, with all the data points agreeing within the 1σ uncertainties. While cross-checks between pipelines are useful to ensure consistency, it is also important to check the robustness and sensitivity of the transmission spectrum obtained using a given pipeline (M. Holmberg & N. Madhusudhan 2024). In the present work, we conduct robustness tests with both pipelines across various considerations in the data reduction and analyses. We discuss some of these results in Appendix A. We demonstrate the robustness of the resultant transmission spectra to a wide range of parameters and assumptions in data reduction and light-curve analyses. These include different treatments for the nonlinearity correction, spectral extraction, spectral binning, and limb darkening, and different trends in the light-curve fitting, as well accounting for correlated noise.

The resulting spectra are consistent within the uncertainties across all these cases, as shown in Appendix A. The corresponding atmospheric constraints are also consistent

Table 2
Retrieved Abundance Estimates and Detection Significances from the MIRI Transmission Spectrum of K2-18 b

Canonical Model	Data	DMS	DMDS	$\ln(\mathcal{Z})$	$\ln(B)$	Detection Significance
DMS Only	JExoRES	$-3.42^{+1.16}_{-1.44}$	⋯	215.45	2.86	DMS (2.9σ)
DMDS Only	JExoRES	⋯	$-3.25^{+1.17}_{-1.30}$	216.40	3.81	DMDS (3.2σ)
DMS + DMDS	JExoRES[a]	<-2.44	$-3.48^{+1.24}_{-2.27}$	216.40	3.80	DMS+DMDS (3.2σ)
DMS Only	JexoPipe	$-3.53^{+1.03}_{-1.33}$	⋯	211.18	3.18	DMS (3.0σ)
DMDS Only	JexoPipe	⋯	$-3.45^{+1.13}_{-1.30}$	211.18	3.17	DMDS (3.0σ)
DMS + DMDS	JexoPipe	$-4.68^{+1.72}_{-4.34}$	$-4.61^{+1.93}_{-4.36}$	211.59	3.59	DMS+DMDS (3.2σ)
Effect of Trend[b]						
DMS + DMDS	JExoRES (Exp+Linear1)[a]	<-2.44	$-3.48^{+1.24}_{-2.27}$	216.40	3.81	DMS+DMDS (3.2σ)
DMS + DMDS	JExoRES (Exp+Linear2)	<-1.81	$-3.67^{+1.59}_{-3.51}$	216.40	2.89	DMS+DMDS (2.9σ)
DMS + DMDS	JExoRES (Exp+Quadratic)	<-2.42	$-3.70^{+1.32}_{-2.82}$	212.92	2.85	DMS+DMDS (2.9σ)
DMS + DMDS	JExoRES (Quadratic)	$-4.56^{+1.52}_{-3.90}$	$-4.89^{+1.87}_{-4.24}$	214.50	4.22	DMS+DMDS (3.4σ)
Masking of Potential Shadow Region[c]						
DMS + DMDS	JExoRES ($\lambda < 10.5\ \mu$m)	<-2.10	$-3.88^{+1.56}_{-4.24}$	168.44	3.51	DMS+DMDS (3.1σ)
DMS + DMDS	JExoRES ($\lambda < 10\ \mu$m)	<-2.15	$-3.46^{+1.23}_{-2.06}$	153.20	3.09	DMS+DMDS (3.0σ)
Accounting for Time-correlated Noise						
DMS + DMDS	JExoRES (no GP)	<-2.16	$-3.72^{+1.38}_{-3.14}$	215.94	4.08	DMS+DMDS (3.3σ)
DMS + DMDS	JExoRES (GP)[a]	<-2.44	$-3.48^{+1.24}_{-2.27}$	216.40	3.81	DMS+DMDS (3.2σ)
Effect of Binning[d]						
DMS + DMDS	JExoRES (0.2 μm)	<-2.16	$-3.72^{+1.38}_{-3.14}$	215.94	4.08	DMS+DMDS (3.3σ)
DMS + DMDS	JExoRES (0.4 μm)	<-2.44	$-2.88^{+0.94}_{-1.97}$	112.72	3.98	DMS+DMDS (3.3σ)
DMS + DMDS	JExoRES (0.8 μm)	<-2.87	$-3.06^{+0.93}_{-1.34}$	63.71	3.79	DMS+DMDS (3.2σ)

Notes. The first column shows the canonical model used with DMS and/or DMDS included. The second column shows the spectrum used from one of the two pipelines, `JExoRES` or `JexoPipe`, along with any specific treatments in the data reduction or light-curve analysis. The DMS and DMDS abundances in the third and fourth columns are shown as $\log_{10}$ of the volume mixing ratios. The retrieved abundances are reported as median values with 1σ uncertainties, for cases with a well-defined peak in the posterior, or as 95% upper limits otherwise. The model evidence is shown for each case as $\ln(\mathcal{Z})$, where $\mathcal{Z}$ is the Bayesian evidence. $\ln(B)$ refers to the natural logarithm of the Bayes factor, comparing the canonical model with a model with DMS and/or DMDS removed. The corresponding molecules are shown in the last column, with their detection significances in parentheses. We note that there is a typical uncertainty of $\sim 0.1\sigma$ in the calculation of the detection significance using MultiNest. GP indicates analysis using Gaussian processes to account for time-correlated noise, as outlined in Appendix A.7.

[a] These correspond to our canonical case presented in Figure 2.

[b] The trend refers to the systematic trend used in the light-curve analysis, as explored in Figure 10. For the two Exp+Linear cases, we remove the first 250 and 500 integrations for Linear1 and Linear2, respectively.

[c] We do not find a strong discontinuity in the detector behavior past 10.6 μm, called the shadow region, sometimes found in MIRI LRS data (T. J. Bell et al. 2024). Nevertheless, we conduct retrievals with different wavelength limits for robustness.

[d] These cases correspond to the spectra presented in Figure 9, which explore the effect of binning. These cases do not use the GP model. For the 0.2 μm case, we use a minimum bin width of 5 pixels, representing our nominal binning as discussed in Section 2.1.

across these cases, as shown in Table 2. We also conduct atmospheric retrievals with spectra from both `JExoRES` and `JexoPipe`, to ensure consistency in the overall conclusions. The abundances and detection significances obtained from each reduction are summarized in Table 2. This is further discussed below.

3. Atmospheric Retrieval

We conduct atmospheric retrievals to derive the properties of the day–night terminator region of the atmosphere of K2-18 b, using the MIRI transmission spectrum. We follow the retrieval approach of previous analyses of JWST observations of K2-18 b (N. Madhusudhan et al. 2023b). We perform atmospheric retrieval using the AURA retrieval framework (A. Pinhas et al. 2019), as implemented in recent works (S. Constantinou et al. 2023; N. Madhusudhan et al. 2023b; S. Constantinou & N. Madhusudhan 2024). The terminator of K2-18 b is modeled as a plane-parallel atmosphere in hydrostatic equilibrium with a nonuniform thermal structure, described using the parametric temperature profile of N. Madhusudhan & S. Seager (2009) with six free parameters. The transmission spectrum is computed considering radiative transfer along the slant path length across the terminator.

The opacity is contributed by molecular line absorption as well as collision-induced absorption due to H_2–H_2 and H_2–He (J. Borysow et al. 1988; G. S. Orton et al. 2007; M. Abel et al. 2011; C. Richard et al. 2012). We consider molecular line opacities from prominent molecules possible in temperate H_2-rich atmospheres, as discussed below, with the volume mixing ratio of each molecule being a free parameter in the model. The atmospheric composition is treated as uniform across the observable photosphere.

We consider a wide range of molecules to explain the features in the observed spectrum. Across the different models considered in this work, we explore 20 molecules, as discussed below and in Appendix B. The model also includes extinction from clouds/hazes, following the parametric prescription outlined in A. Pinhas et al. (2019), involving four free parameters corresponding to a cloud-top pressure, amplitude, and power-law slope of a Rayleigh-like haze, as well as a coverage fraction. Other free parameters in the model include a reference pressure ($P_{\rm ref}$) corresponding to the white-light planet radius, using the stellar radius from B. Benneke et al. (2019), and a constant vertical offset added to the spectrum from a given instrument, in this case MIRI LRS. We note that the offset is degenerate with $P_{\rm ref}$. Nevertheless, we include both parameters to maintain uniformity in analyses with prior works, and in case an offset is needed that is greater than the allowed pressure range for $P_{\rm ref}$. In total, the number of free parameters in a typical model is $N = N_{\rm mol} + 12$, where $N_{\rm mol}$ is the number of molecules.

The Bayesian inference and parameter estimation is conducted using the nested sampling algorithm (J. Skilling 2004), through the MultiNest implementation (F. Feroz et al. 2009; J. Buchner et al. 2014). Across our retrievals, we use 2000 live points, ensuring fine sampling of the parameter space and accurate estimation of the Bayesian evidence. For robustness, we also perform several of the canonical retrievals discussed below, using the `UltraNest` implementation (J. Buchner 2021), as used in the VIRA retrieval framework, the most recent variant of AURA (S. Constantinou & N. Madhusudhan 2024).

3.1. Retrieval Setup and Model Selection

The present transmission spectrum is the first mid-infrared (~6–12 μm) transmission spectrum of a candidate hycean world ever observed. Given the wide range of molecules that could contribute spectral features in this range, we follow a hierarchical Bayesian approach to determine the preferred model for explaining the observations. We carry out the model selection in two stages, with the model parameters in the retrieval at the second stage being informed by the first stage, as discussed below. At the end, the preferred model given the data is chosen by comparing the Bayesian evidence between the two stages.

We first conduct a maximal retrieval using the `JExoRES` spectrum, with an atmospheric model that includes a substantially expanded set of molecules over previous atmospheric retrievals of K2-18 b. We consider 20 molecules, including 11 molecules considered in previous work (N. Madhusudhan et al. 2023b) and nine new ones. The previous molecules include H_2O, CH_4, NH_3, CO, CO_2, HCN, $(CH_3)_2S$ (DMS), CH_3Cl, CS_2, OCS, and N_2O. The molecules H_2O, CH_4, NH_3, CO, CO_2, and HCN have been predicted to be the prominent C-, O-, and N-bearing species in temperate H_2-rich atmospheres, including hycean worlds (e.g., R. Hu 2021; N. Madhusudhan et al. 2021; X. Yu et al. 2021). The remaining molecules $(CH_3)_2S$ (DMS), CH_3Cl, CS_2, OCS, and N_2O have been predicted as observable potential biosignatures in H_2-rich atmospheres of habitable super-Earths (A. Segura et al. 2005; S. D. Domagal-Goldman et al. 2011; S. Seager et al. 2013a) and hycean worlds (N. Madhusudhan et al. 2021).

The new molecules include other prominent sulfur-based molecules, hydrocarbons, and potential biomarkers (e.g., C. Sousa-Silva et al. 2020; E. W. Schwieterman & M. Leung 2024; S.-M. Tsai et al. 2024): H_2S, SO_2, C_2H_2, C_2H_4, C_2H_6, $(CH_3)_2S_2$ (dimethyl disulfide; DMDS), CH_3SH, PH_3, and CH_3OH. Of these molecules, DMDS, CH_3SH, C_2H_6, and PH_3 are particularly relevant as potential biomarkers both in hycean as well as terrestrial-like atmospheres, as suggested in recent studies (e.g., C. Sousa-Silva et al. 2020; E. W. Schwieterman & M. Leung 2024; S.-M. Tsai et al. 2024). Of all the molecules considered, DMS, DMDS, CH_3SH, CH_3Cl, and N_2O are expected to be the most reliable biosignatures in hycean conditions, whereas others may have alternate abiotic sources (A. Segura et al. 2005; S. D. Domagal-Goldman et al. 2011; S. Seager et al. 2013a; E. W. Schwieterman & M. Leung 2024; S.-M. Tsai et al. 2024).

The retrieval obtains a good fit to the spectrum, with the model being inconsistent with a featureless spectrum, i.e., a flat line, at 3σ significance. However, an inspection of the posteriors reveals only one well-constrained peak for the molecule DMDS, while all the other molecules are unconstrained, as shown in Appendix B. We also do not find significant constraints for cloud/haze parameters that could affect the mid-infrared spectrum.

We further conduct a retrieval without DMDS and find a well-constrained peak in the posterior for DMS. We find that DMS replaces DMDS, due to the strong degeneracy between the two molecules in the MIRI wavelength range where prominent peaks are evident in the data, as shown in Figure 2. The spectral contributions due to the two molecules are shown in Figure 4. Thus, the retrievals highlight the degeneracy between DMS and DMDS, with a higher preference for DMDS from this data set. On removing both molecules from the retrieval, we find no significant constraints on any of the remaining molecules. The model without DMS and DMDS does not provide a good fit to the data, with the maximal model preferred over this model at 2σ. Moreover, the model without DMS and DMDS is only marginally favored over a flat spectrum below 2σ significance. The data therefore show notable evidence for only two molecules, DMDS and DMS.

Informed by the above retrieval, we arrive at a canonical model that includes DMS and DMDS. We additionally include CH_4 and CO_2, which have been detected in K2-18 b previously in the near-infrared (N. Madhusudhan et al. 2023b). In total, our canonical model includes 16 free parameters: four molecular mixing ratios, six for the P–T profile, four for the cloud parameters, one for $P_{\rm ref}$, and one for the offset on the MIRI data. The retrieval with this model provides a comparable fit to the data as the maximal model above, but with a higher Bayesian evidence, due to the lower number of unconstrained free parameters. The canonical model is preferred over the maximal model by 2.2σ and over a featureless spectrum, i.e., a flat line, by $\geqslant 3.4\sigma$. For computing the Bayesian evidence for the one-parameter model of a featureless spectrum, we assume uniform priors on the model transit depth, with a range of $\pm N$ ppm relative to the measured white-light transit depth. Considering the span of transit depths in the observed spectrum of ~600 ppm, we explore values of N between 600–2000 ppm. Over this range, the canonical model is preferred over a featureless spectrum at 3.4σ–3.8σ, with higher preferences obtained for wider priors, i.e., larger N. We adopt the minimum preference of 3.4σ as a conservative estimate.

As with the maximal model, we find that only DMDS is constrained by this data set, while other parameters remain unconstrained. We also recover the degeneracy between DMDS and DMS, such that when DMDS is excluded from the model, DMS is recovered. In what follows, we present the detection significances of the molecules and atmospheric

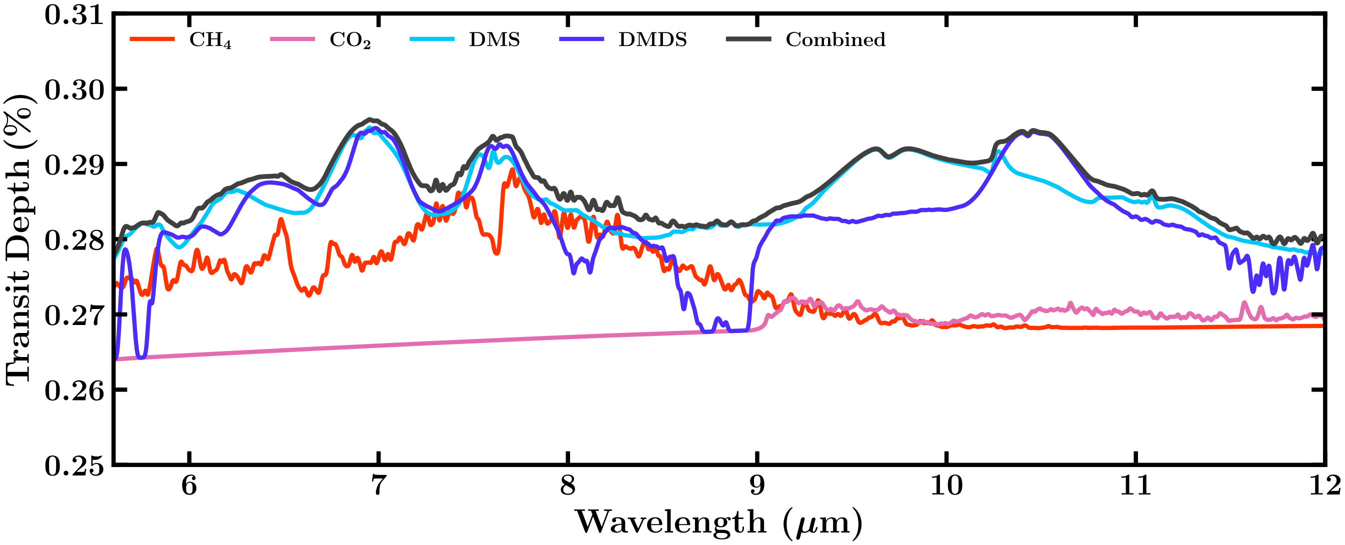

Figure 4. Spectral contributions of notable chemical species in the MIRI band. Each curve denotes the spectral contribution of a particular molecule to the model spectrum, as denoted in the legend. The mixing ratios of DMS and DMDS are set to a representative value of 5×10^{-4}, while CH_4 and CO_2 are set to 10^{-2}, consistent with constraints obtained from previous near-infrared observations (N. Madhusudhan et al. 2023b). The black line denotes the resulting transmission spectrum with all molecular contributions combined.

constraints with the canonical model using the spectra obtained from both pipelines.

3.2. Atmospheric Constraints

The spectrum provides important insights into the atmospheric composition of K2-18 b. The retrieved spectral fit along with the 1σ and 2σ contours using the `JExoRES` spectrum is shown in Figure 2. As noted above, the present MIRI spectrum spans a wavelength range of ∼5.8–12 μm, which encompasses strong spectral features of several prominent molecules expected in temperate H_2-rich atmospheres, as shown in Figures 4 and 14. However, as discussed above, we are unable to explain the observed features with most of the 20 prominent species considered, with the maximal retrieval finding no significant evidence for 18 of the 20 species. The only species with notable evidence are DMDS and DMS. Both molecules have a similar double-peak feature between 6.8 and 8 μm, with additional broad peaks around 9.8 μm and 10.5 μm for DMS and DMDS, respectively, which are consistent with the observed spectrum. Additionally, the amplitudes of the observed spectral features, of ∼300–400 ppm, in the present MIRI data are significantly larger compared to the ∼200 ppm amplitudes seen in previous near-infrared (∼1–5 μm) observations with the NIRISS and NIRSpec instruments (N. Madhusudhan et al. 2023b). While previous observations detected strong spectral features of CH_4 and CO_2 in the near-infrared, neither of them are detectable in the present spectrum, as can be seen in Figure 4. While CO_2 does not have strong spectral features in the MIRI LRS range, those of CH_4 are dwarfed by stronger contributions due to DMS and/or DMDS. As such, the contributions of both CO_2 and CH_4 at previously reported mixing ratios (∼1%) are insufficient to explain the present data in the MIRI band, as can be seen in Figure 4. Instead, contributions from DMDS and DMS at volume mixing ratios of $\sim 10^{-5}$–10^{-3} readily explain the data, due to their strong absorption cross sections in the MIRI band.

The spectrum provides notable constraints on the presence and abundance of DMDS and DMS in the atmosphere, as shown in Figure 5. Due to the degeneracy between the spectral features of DMDS and DMS in the MIRI band, as shown in Figure 4, it is difficult to robustly distinguish between them at the current data quality. Considering the canonical model, where both DMDS and DMS are present, DMDS is preferred at a somewhat higher significance ($\sim 2\sigma$) compared to DMS for the `JExoRES` spectrum. The presence of DMDS in the model is favored at 2σ significance compared to the model without DMDS. DMS is not well constrained, and the model with DMS is preferred over the model without DMS at only 1σ significance. The lack of either molecule in the model is compensated for by the other, due to the degeneracy in their spectral features, as discussed above. However, the combination of DMDS and DMS together is favored at 3.2σ over a model with neither molecule included (Table 2).

On the other hand, retrievals with models including only one of the two molecules at a time show relatively high detection significances for both molecules individually. For example, considering the canonical model with only DMDS included, i.e., DMS removed, we find that the detection significance for DMDS is 3.2σ. Similarly, the canonical model with only DMS included, i.e., DMDS removed, provides a detection significance for DMS of 2.9σ. Therefore, the present data provide evidence for the presence of DMDS and/or DMS at 2.9σ–3.2σ significance.

The retrieved posterior distributions for the volume mixing ratios of DMDS and DMS shown in Figure 5 reflect the degeneracy between the two species that is apparent from their spectral contributions, as discussed above. When both molecules are included in the model, the spectral contribution of DMDS dominates over that of DMS. The posterior of DMDS shows a clear peak, albeit with a low-abundance tail, due to the degeneracy with DMS. The abundance of DMDS is retrieved to be $\log(X_{\mathrm{DMDS}}) = -3.48^{+1.24}_{-2.27}$, while DMS is unconstrained. Here, X_{DMDS} is the volume mixing ratio of DMDS. In retrievals with only one of the two molecules present, the posterior of that molecule shows a single well-constrained peak with no low-abundance tail. In such retrievals, the abundances are retrieved to be $\log(X_{\mathrm{DMDS}}) = -3.25^{+1.17}_{-1.30}$ and $\log(X_{\mathrm{DMS}}) = -3.42^{+1.16}_{-1.44}$, as shown in Table 2. Last, we repeat the canonical retrieval using the UltraNest nested

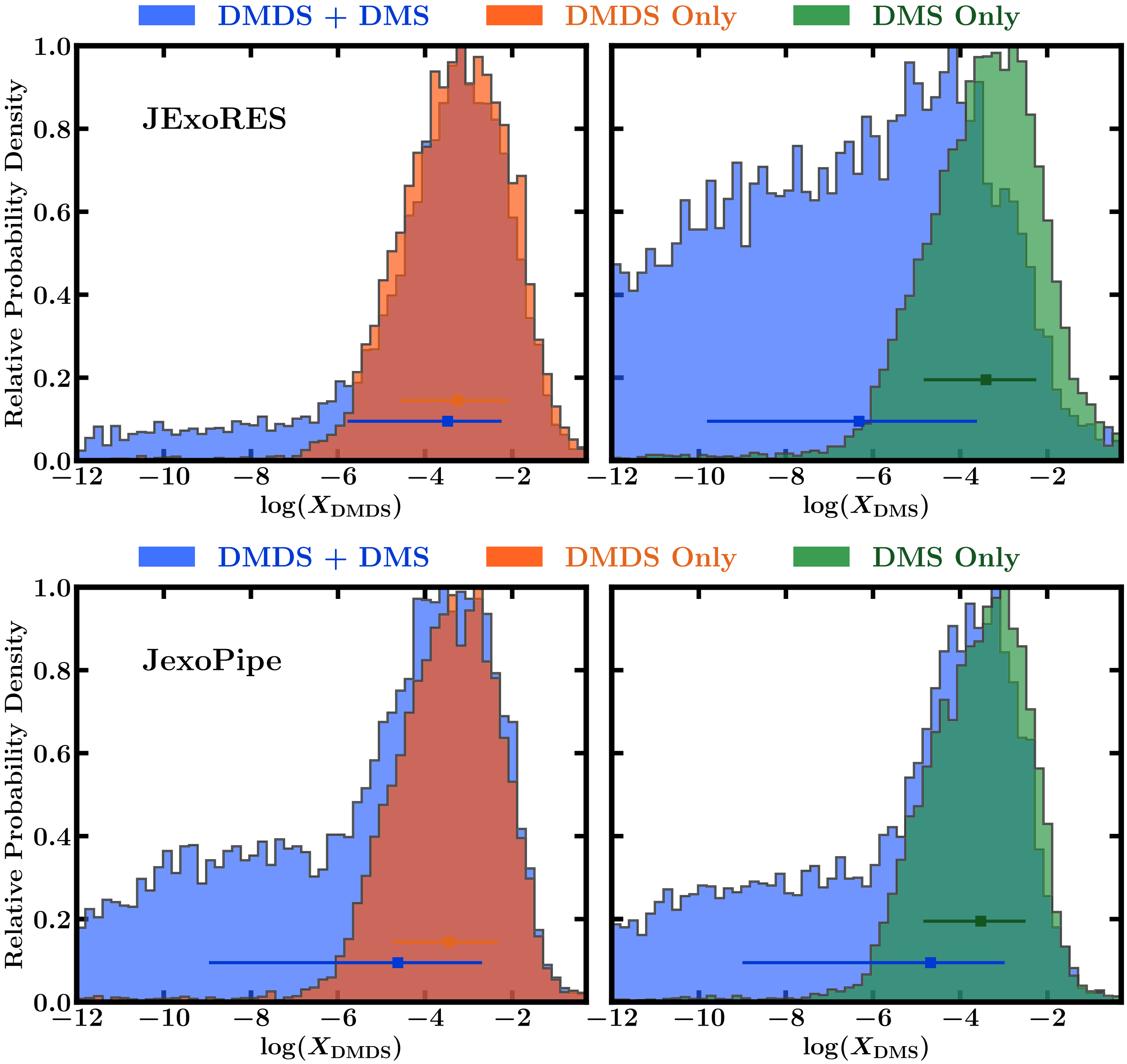

Figure 5. Retrieved posterior probability distributions for DMDS and DMS from our canonical retrievals described in Section 3, using data from the `JExoRES` (top) and `JexoPipe` (bottom) pipelines. The posteriors shown in blue correspond to the canonical retrieval containing both DMDS and DMS, along with CH_4 and CO_2. The other two cases show the retrievals with only one of the two molecules, DMDS or DMS, included in the canonical retrieval, with all other parameters remaining unchanged. The orange distribution corresponds to the retrieval with only DMDS present, and the green distribution corresponds to the retrieval with only DMS present.

sampling implementation and find consistent abundance estimates and detection significances to our standard retrievals using the MultiNest implementation.

We also conduct another canonical retrieval with our other spectrum obtained with the `JexoPipe` pipeline. We find that the detection significances and abundance estimates of DMS and DMDS are consistent with those obtained using the `JExoRES` spectrum, as shown in Table 2. We find the combined detection significance of DMDS and DMS to be 3.2σ, similar to that obtained with the canonical retrieval with the `JExoRES` data. The abundances are slightly lower but still consistent. For this canonical model, where DMS and DMDS are both included, the posteriors for DMS and DMDS are comparable, as shown in Figure 5. Using the individual DMS-only or DMDS-only cases, we find evidence for each of the molecules at 3σ significance and similar abundance estimates to the corresponding `JExoRES` cases: $\log(X_{\rm DMDS}) = -3.45^{+1.13}_{-1.30}$ and $\log(X_{\rm DMS}) = -3.53^{+1.03}_{-1.33}$. Therefore, across all our retrievals, we detect DMDS and/or DMS at 3σ significance.

The observations do not provide significant constraints on any of the other molecules or atmospheric properties but are consistent with previous inferences from the near-infrared JWST spectrum (N. Madhusudhan et al. 2023b). Specifically, we do not obtain significant constraints on CH_4 or CO_2, which have previously been detected. However, the upper limits we retrieve for the abundances of both molecules are consistent with their previous abundance estimates. The contributions from both molecules at previously measured abundances of $\sim$1% each are insufficient to explain the observed spectral

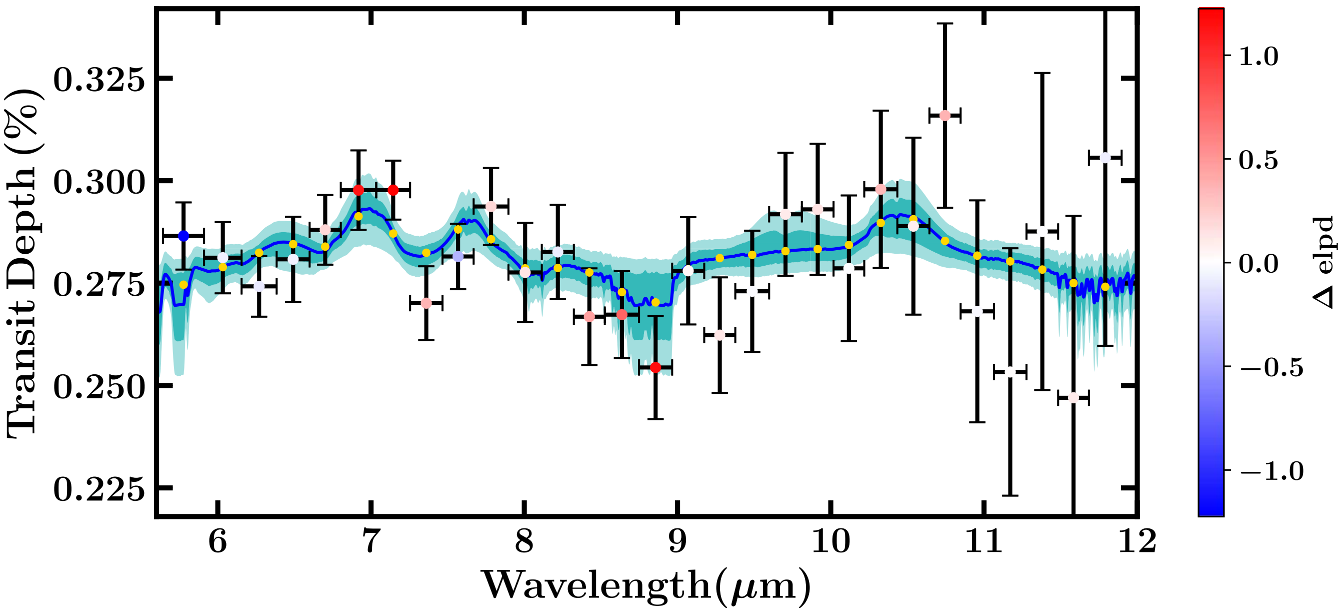

Figure 6. Leave-one-out analysis for the MIRI transmission spectrum of K2-18 b. The black data points with error bars show the observed transmission spectrum obtained using the `JExoRES` pipeline. The center shading of each data point denotes the corresponding elpd difference (Δelpd) between the canonical atmospheric model with DMS and DMDS and one with both molecules absent. The redder points denote higher and positive Δelpd, indicating that the canonical model is more capable of predicting them if they are absent from the fit than the atmospheric model without DMS and DMDS. Similarly, bluer points denote larger negative Δelpd values, indicating a preference against DMS and DMDS, while white points denote Δelpd values close to zero. Gold points denote the median retrieved spectrum (in blue) binned for each data point, while the dark and light cyan shaded regions denote the retrieved 1σ and 2σ contours, respectively.

features in the present spectral range with JWST MIRI (6–12 μm). While CO_2 has no strong spectral features in this range, those of CH_4 are significantly weaker compared to those of DMDS and/or DMS, as shown in Figure 4. The abundances we retrieve for DMS and/or DMDS are also consistent with the constraints for DMS reported in previous work.

Similarly, we do not find significant evidence for spectral contributions due to clouds/hazes in the MIRI band and none of the cloud parameters are constrained. We find the photospheric pressure corresponding to the white-light radius to be $\log(P_{\rm ref}/{\rm bar}) = -4.32^{+1.15}_{-0.93}$, with no significant offset to the data retrieved. The offset is retrieved to be 12^{+51}_{-58} ppm, which is consistent with zero within the 1σ uncertainties. The photospheric temperature at 1 mbar at the terminator is also weakly constrained to be 422^{+141}_{-133} K, which is somewhat higher but consistent with previous estimates in the near-infrared to within 1σ uncertainties.

For additional robustness, we conduct retrievals on the transmission spectra obtained using a wide range of assumptions for the data reduction and analyses. Using `JExoRES`, we explore differences in the treatment of systematic trends and time-correlated noise, as well as different wavelength limits and the effect of spectral binning, as discussed in Appendix A. Across all of these cases, we find consistent abundance constraints and detection significances of DMDS and/or DMS, ranging from 2.9σ to 3.4σ, as outlined in Table 2.

3.3. Leave-one-out Analysis

As a further robustness check for our findings, we carry out leave-one-out cross-validation using the `JExoRES` data. We follow A. Vehtari et al. (2017) and L. Welbanks et al. (2023), calculating the expected log pointwise predictive density (elpd) for each data point. For each data point d_i, we carry out an atmospheric retrieval with all other points considered and that data point removed. We do not make any approximations, e.g., Pareto-smoothed importance sampling, and instead directly compute the elpd of each data point by carrying out a retrieval considering all other data points. Using the retrieved posterior samples, we compute the probability density of the ith point d_i, given a retrieval using model $\mathcal{M}$ on all other data d_{-i}, resulting in a total of S samples of the parameter space for each retrieval. The elpd metric provides an indication of how well each data point can be predicted by the model and therefore quantifies the performance of the model. The metric is given by

$$\begin{aligned}\mathrm{elpd}_{i,\mathcal{M}} &= \log\left(p(y_i|y_{-1}, \mathcal{M})\right)\\ &= \log\left(\frac{1}{S}\sum_{j=1}^{S} p(y_i|\theta_j, \mathcal{M})\right),\end{aligned} \quad (1)$$

where the parameters corresponding to the jth sample in each retrieval are denoted as θ_j. We perform the above calculation for two atmospheric models: the canonical model described in Section 3 and one with DMS and DMDS absent. As such, we run a total of two retrievals per data point. The difference between the elpd values of the two models, $\Delta\mathrm{elpd}_i$, indicates their relative performance. Conversely, in this case, $\Delta\mathrm{elpd}_i$ serves as an indication for the relative contributions of the data points toward the present detection of DMDS and DMS. The pointwise $\Delta\mathrm{elpd}_i$ is shown in Figure 6. We find that most points have $\Delta\mathrm{elpd}_i$ values above zero, indicating that the detection of DMDS and DMS combined is driven by multiple data points to various extents. $\Delta\mathrm{elpd}_i$ is highest for two data points near 7 μm and another two points just under 9 μm. This indicates that these points are better predicted by a model that includes DMDS and DMDS than a model without the two molecules. Conversely, the data point below 6 μm has the most negative $\Delta\mathrm{elpd}_i$, indicating that it is better predicted by a model without DMS and DMDS. Overall, our leave-one-out analysis indicates that the present detection is unlikely to be the result of localized systematics or individual outlier points.

4. Summary and Discussion

We report a mid-infrared transmission spectrum of the candidate hycean world K2-18 b observed with the JWST MIRI LRS instrument, the first for a habitable-zone sub-Neptune. The spectrum shows multiple spectral features between ∼6 and 11 μm that are best explained by a combination of DMDS and DMS in the atmosphere, both molecules uniquely produced by life on Earth and predicted as promising biosignatures in habitable exoplanets (S. D. Domagal-Goldman et al. 2011; S. Seager et al. 2013b; D. C. Catling et al. 2018; E. W. Schwieterman et al. 2018; S.-M. Tsai et al. 2024). We detect the combination of DMDS and/or DMS at a significance of 2.9σ–3.2σ across the canonical retrievals reported in this work. In the absence of DMDS, the spectral features can also be explained to a large extent by DMS, and vice versa, due to degeneracy between the spectral features of DMS and DMDS in the mid-infrared. In retrievals considering only one of the two molecules (DMS or DMDS) in the canonical model, DMS is retrieved at 2.9σ–3.0σ significance and DMDS is retrieved at 3.0σ–3.2σ significance.

The observations provide limited constraints on other atmospheric properties. In the absence of DMS and DMDS, no significant detections or abundance constraints are obtained on any of the remaining molecules considered in the retrievals. The strong DMDS and/or DMS features dominate over potential molecular contributions from any other species in this wavelength range. We find high abundances of DMDS and/or DMS with volume mixing ratios of $\gtrsim 10^{-5}$ (10 ppmv) within the 1σ uncertainties and a MIRI photospheric temperature of 422^{+141}_{-133} K at 1 mbar for the canonical retrieval. The DMS abundance and photospheric temperature are consistent with but somewhat higher than those derived from previous NIRISS and NIRSpec observations in the 1–5 μm region (N. Madhusudhan et al. 2023b). On the other hand, both the retrieved mixing ratios and temperature are strongly dependent on the available cross sections of DMDS and DMS that are obtained for an Earth-like atmosphere at nearly STP conditions, using N_2 as a broadener (I. Gordon et al. 2017). Therefore, the derived abundances and temperatures may be impacted by the assumed collisional broadening factors and/or the adopted molecular cross sections, in general.

Overall, our findings continue to raise the prospect of possible biological activity on K2-18 b and motivate new experimental and theoretical work for detailed characterization of its atmospheric properties. In what follows, we discuss the implications and future directions.

4.1. Biosignature on a Hycean World

Our findings provide new independent evidence for the possibility of a biosphere on K2-18 b. As discussed in Section 1, the detection of carbon-bearing molecules, CH_4 and CO_2, and nondetections of NH_3 and CO (N. Madhusudhan et al. 2023b) are consistent with prior predictions for a hycean world and inconsistent with mini-Neptune or gas dwarf scenarios (G. J. Cooke & N. Madhusudhan 2024; F. E. Rigby et al. 2024). The previous observations also showed tentative hints of DMS, a possible biosignature molecule in the atmosphere (N. Madhusudhan et al. 2023b), but the evidence was weak. This new independent evidence for the presence of DMS and/or DMDS at 2.9σ–3.2σ adds to the tentative inference of DMS reported previously and bolsters the chances of a biosphere on K2-18 b.

Recent photochemical modeling of K2-18 b suggests that large quantities of DMS and DMDS, with mixing ratios up to 10^{-2}, can accumulate in the atmosphere for assumed biogenic oceanic fluxes of these gases of $\gtrsim 20$ times Earth levels (S.-M. Tsai et al. 2024). Such quantities are consistent with our current MIRI results for DMDS and DMS and with previous abundance constraints of DMS (N. Madhusudhan et al. 2023b). These otherwise photochemically fragile molecules survive in the S.-M. Tsai et al. (2024) models under high-surface-flux-emission conditions: (1) because of the favorable ultraviolet spectral energy distribution of M dwarf stars (see also A. Segura et al. 2005; S. D. Domagal-Goldman et al. 2011; S. Seager et al. 2013a); (2) because DMS and DMDS can eventually self-shield, as well as shield molecules such as CO_2 from photolysis, when their column density is high enough, significantly cutting down on their photochemical destruction pathways (S.-M. Tsai et al. 2024); and (3) because the models assume that biogenically emitted DMS and DMDS do not have a return sink to the ocean, allowing the abundance to build up over time. Our present MIRI abundance estimates of DMS and/or DMDS at mixing ratios of $\sim 10^{-5}$–10^{-3} could, therefore, imply stronger biological activity on the planet in comparison to Earth. We note however, that DMDS could potentially condense on K2-18 b (see C. Sagan & B. N. Khare 1971; B. N. Khare et al. 1978; D. M. VonNiederhausern et al. 2006), depending on tropopause temperatures, restricting its gas-phase abundance in the stratospheric region that is probed in the transit observations. Therefore, abundances significantly higher than $\sim 10^{-4}$–10^{-3} may be difficult to achieve if the stratosphere is too cold.

On the other hand, it is possible that the abundance estimates derived in our work are strongly influenced by the uncertainties in spectral parameters and cross sections of these molecules used in the models. The derived abundance and temperature are strongly dependent on the absorption cross section of a molecule detected. For both DMDS and DMS, only limited cross sections are available in the literature (I. Gordon et al. 2017), which are derived experimentally, assuming an Earth-like N_2-rich background atmosphere at nearly STP conditions. It is possible that the collisional broadening factors and cross sections may be different for an H_2-rich background gas at lower pressures probed in the present transmission spectroscopy. Therefore, our results highlight the acute need for laboratory and theoretical work to derive high-fidelity absorption cross sections for these and other biosignature molecules, to enable their robust detection and abundance estimates in habitable exoplanets.

4.2. False Positives

As with any potential biosignature molecule, it is important to ask whether there can be abiotic sources of DMS and DMDS in a temperate H_2-rich atmosphere that could explain the observations. Both DMS and DMDS have been predicted to be robust biosignatures for Earth-like planets as well as planets with H_2-rich atmospheres, including super-Earths and hycean worlds (S. D. Domagal-Goldman et al. 2011; S. Seager et al. 2013a; D. C. Catling et al. 2018; E. W. Schwieterman et al. 2018;

N. Madhusudhan et al. 2021). Their identification as robust biosignatures is due to the fact that on Earth, both molecules are uniquely produced by life (particularly marine biota) in small quantities of $\lesssim 1$ ppb by volume and are not supplied by abiotic photochemistry. Nevertheless, here we explore some potential alternatives.

Experimental studies have demonstrated the feasibility of forming several organosulfur compounds abiotically, using ultraviolet irradiation or electric discharges of gaseous mixtures containing H_2S and CH_4 (e.g., F. Raulin & G. Toupance 1975; C. He et al. 2020; V. Vuitton et al. 2021; N. W. Reed et al. 2024). In particular, some of these studies have demonstrated the production of both DMS (F. Raulin & G. Toupance 1975; N. W. Reed et al. 2024) and DMDS (C. Sagan & B. N. Khare 1971; B. N. Khare et al. 1978) in gas mixtures containing both CH_4 and H_2S, arguing in favor of their possible abiotic production in reduced planetary atmospheres. However, both DMS and DMDS are highly reactive and have very short lifetimes in the above experiments (e.g., a few minutes) and in the Earth's atmosphere (between a few hours to $\sim$1 day), due to various photochemical loss mechanisms (e.g., S. Seager et al. 2013b). Thus, the resulting DMS and DMDS mixing ratios in the current terrestrial atmosphere are quite small (typically $\lesssim 1$ ppb), despite continual resupply by phytoplankton and other marine organisms.

Therefore, sustaining DMS and/or DMDS at over 10–1000 ppm concentrations in a steady state in the atmosphere of K2-18 b would be implausible without a significant biogenic flux. Moreover, the abiotic photochemical production of DMS in the above experiments requires an even greater abundance of H_2S as the ultimate source of sulfur—a molecule that we do not detect—and requires relatively low levels of CO_2 to curb DMS destruction (N. W. Reed et al. 2024), contrary to the high reported abundance of CO_2 on K2-18 b (N. Madhusudhan et al. 2023b).

Another recent study has reported evidence for the presence of DMS on the comet 67P/Churyumov–Gerasimenko (N. Hänni et al. 2024), motivating the possibility of a potential abiotic source through cometary delivery to the exoplanet's atmosphere. Comets are also known to contain other ices and sublimated gases that might be considered biosignatures if present in an exoplanet atmosphere, including O_2, CH_4, and CH_3Cl (A. Bieler et al. 2015; E. C. Fayolle et al. 2017; M. Rubin et al. 2019). However, cometary delivery is implausible for explaining such molecules in planetary atmospheres, due to the insufficient contribution that trace species within a comparatively small comet would add to the much more massive planetary atmosphere (e.g., R. W. Court & M. A. Sephton 2012; R. C. Felton et al. 2022; M. Leung et al. 2022). Moreover, molecules such as DMS and DMDS would be shock-heated during a hypervelocity cometary impact and its related plume splashback phase, which would reset the bulk composition to simpler molecules that are more stable in thermochemical equilibrium at high temperatures and (for the splashback phase) low pressures (K. Zahnle 1996). Therefore, DMS and DMDS would not be delivered at any significant measurable levels through such a process. We also note that DMDS has not been reported in the comet 67P. In summary, cometary impacts cannot be responsible for the relatively large DMS and/or DMDS abundances inferred from the present MIRI retrievals.

4.3. Future Directions

A conclusive identification of a biosignature necessitates a robust assessment of various factors, including the robustness of the detections, the environmental context, and potential false positives (e.g., E. W. Schwieterman et al. 2018; V. Meadows et al. 2022). It is widely recognized that the detection of a biosignature is unlikely to be instantaneous or unambiguous in the first instance, rather relying on continued accumulation of evidence and addressing the above factors (V. Meadows et al. 2022). Our study is the first formal step in this direction, building on the first possible hints of DMS reported in our previous work (N. Madhusudhan et al. 2023b) and the further evidence of DMDS and/or DMS with a higher significance seen in the present observations. Finally, our present detection, based on multiple spectral features with a different instrument in a different spectral range from previous work, provides an important independent line of evidence in this direction.

Further work is needed to robustly verify the current findings. More observations are required to robustly demonstrate the repeatability of our present findings, rule out potentially unaccounted-for instrumental systematics, as well as increase the detection significances. While DMDS and DMS best explain the current observations, their combined detection significance is $\sim 3\sigma$, which is at the lower end of the robustness typically required for scientific evidence. The significance can be readily increased to a 4σ–5σ level by a modest amount of additional JWST time, e.g., between one and three additional transits with MIRI, i.e., only $\sim$8–24 hr. Second, while we have explored 20 prominent molecules in fitting the spectrum, our search may still not be fully exhaustive. Therefore, future studies could investigate other potential molecules that could explain the data. At the same time, as discussed above, new experimental and theoretical studies are needed to determine accurate absorption cross sections for DMDS and DMS, and other potential biosignature molecules, for conditions relevant to candidate hycean worlds like K2-18 b. Future laboratory experiments and/or theoretical modeling are also needed to fully explore the possible photochemical mechanisms for producing DMS and DMDS in dry, methane-rich, reduced environments, to address potential abiotic sources of these molecules.

Overall, our findings present an important step forward in the search for signatures of life on exoplanets. However, robustly establishing both the veracity of the present findings and their possible association with life on K2-18 b needs a dedicated community effort in multiple directions—observational, theoretical, and experimental. Observations with JWST are already demonstrating that possible hycean worlds indeed significantly expand and accelerate the search for life elsewhere. The central question now is whether we are prepared to identify the signatures of life on such worlds. The opportunity is at our doorstep.

Acknowledgments

This work is based on observations made with the NASA/ESA/CSA James Webb Space Telescope as part of Cycle 1 GO Program 2722 (PI: N. Madhusudhan). We thank NASA, ESA, CSA, STScI, and everyone whose efforts have contributed to the JWST, as well as the exoplanet science community for the thriving current state of the field. This work is supported by a UK Research and Innovation (UKRI) Frontier

Research grant (EP/X025179/1); PI: N. Madhusudhan. N.M. thanks Tony Roman and Sara Kendrew at STScI for their help with planning our JWST observations. J.M. acknowledges support from JWST-GO-02722, which was provided by NASA through a grant from the Space Telescope Science Institute, which is operated by the Association of Universities for Research in Astronomy, Inc., under NASA contract NAS 5-03127. We thank the anonymous reviewer for the valuable comments on the manuscript.

This work was performed using resources provided by the Cambridge Service for Data Driven Discovery operated by the University of Cambridge Research Computing Service (www.csd3.cam.ac.uk), provided by Dell EMC and Intel, using Tier-2 funding from the Engineering and Physical Sciences Research Council (capital grant EP/P020259/1) and DiRAC funding from STFC (www.dirac.ac.uk).

Author Contributions

N.M. conceived, planned, and led the project. N.M. led the JWST proposal, with contributions from S.C., S.S., A.P., and J. M. N.M., S.S., and M.H planned the JWST observations. N.M., M.H., and S.S. conducted the data reduction and spectroscopic analyses. N.M. and S.C. conducted the atmospheric retrievals. N.M. and J.M. conducted the theoretical interpretation. N.M. led the writing of the manuscript, with contributions and comments from all authors.

Data Availability

The spectra obtained with the `JExoRES` and `JexoPipe` pipelines, along with the retrieved posterior distributions for the canonical model retrievals, are available at https://osf.io/gmhw3/. The JWST data presented in this article were obtained from the Mikulski Archive for Space Telescopes at the Space Telescope Science Institute. The specific observations analyzed can be accessed via doi:10.17909/rx29-yw62.

Facility: JWST (MIRI).

Appendix A
Robustness of Transmission Spectra

A.1. Comparison between Pipelines

In this work, we thoroughly test several data reduction methods and assumptions—such as the effect of the nonlinearity correction, the choice of binning, detrending, and limb darkening—to produce a robust transmission spectrum. We also apply two independently developed data reduction pipelines to check for consistency, using `JExoRES` and `JexoPipe`, as described in Sections 2.1 and 2.2, respectively. Figure 3 demonstrates the stability of the MIRI transmission spectrum of K2-18 b when comparing these two pipelines. Table 1 provides the parameters from the white-light-curve fitting with both pipelines, yielding results consistent within 1σ.

A.2. Nonlinearity Correction

We explored how differences in nonlinearity correction can affect the transmission spectrum, as pursued in recent works (D. Grant et al. 2023; E. M. R. Kempton et al. 2023; A. Dyrek et al. 2024). As the baseline case, we use the standard nonlinearity corrections, RSCD correction, and dark subtraction. Note that the RSCD correction step does not alter the raw data. Instead, it applies a mask to the first few groups—removing these from the ramp fitting. On the other hand, the dark reference file includes both the dark signal and the RSCD effect, which are corrected by applying the dark subtraction step. For our custom approach, we empirically derive our own RSCD and nonlinearity correction. Using the average of the last 500 (out-of-transit) integrations of our observation, accounting for outliers, we first fit the ramp of each pixel using

$$f(t) = p_1 + p_2 t + p_3 t^2 - p_4 \exp(-t/p_5)\,, \tag{A1}$$

where t is the time since the start of an integration. Here, p_1 corresponds to an overall offset/bias, p_2 is the linear part of the signal that we use to represent the true flux (J. E. Morrison et al. 2023), p_3 is the quadratic nonlinear component representing the change in response as the charge accumulates, p_4 is the strength of the RSCD signal, and p_5 is the timescale of the RSCD signal. For this fit, we exclude the first and last group, as done in the main analysis described in Sections 2.1 and 2.2. Next, we subtract the RSCD correction, including the constant term, i.e.,

$$f_{\rm reset}(t) = p_1 - p_4 \exp(-t/p_5)\,, \tag{A2}$$

from the data before applying our custom nonlinearity correction. We derive the parameters for the nonlinearity correction using a fourth-degree polynomial h, defined as

$$h(p_2 t + p_3 t^2) = p_2 t\,,\; h(x) = \sum_{i=0}^{4} a_i x^i\,, \tag{A3}$$

where a_i, being pixel-dependent, is used to populate the custom nonlinearity reference file. Because we have already subtracted the RSCD signal, we do not apply the dark subtraction step in this scenario.

Following this custom nonlinearity correction approach, we perform the rest of the analysis as outlined in Section 2.1. Figure 7 shows the transmission spectrum of K2-18 b using the standard and custom nonlinearity correction. Overall, we find that the spectrum is largely insensitive to the choice of nonlinearity correction. We note that other data sets may be more sensitive to the nonlinearity correction if the flux level is higher (for the present observation, it is below 51% saturation) or for targets with a larger transit depth than K2-18 b.

A.3. Spectral Extraction Method

We also check if the choice of spectral extraction method significantly affects the MIRI transmission spectrum of K2-18 b. Nominally, we adopt the optimal extraction method (K. Horne 1986), as outlined in Sections 2.1 and 2.2, which is commonly used in the literature (e.g, J. Bouwman et al. 2023; E. M. R. Kempton et al. 2023; T. J. Bell et al. 2024; A. Dyrek et al. 2024). Additionally, we also perform box extraction, where each pixel in the aperture is given equal weighting. For this, we use an aperture of 9 pixels, the same as for the optimal extraction. We find that the transmission spectrum is consistent between the two methods, as shown in Figure 8. The box extraction method produces somewhat larger uncertainties toward the red part of the spectrum compared to optimal extraction (around 15% larger), as expected, given the lower throughput in this region.

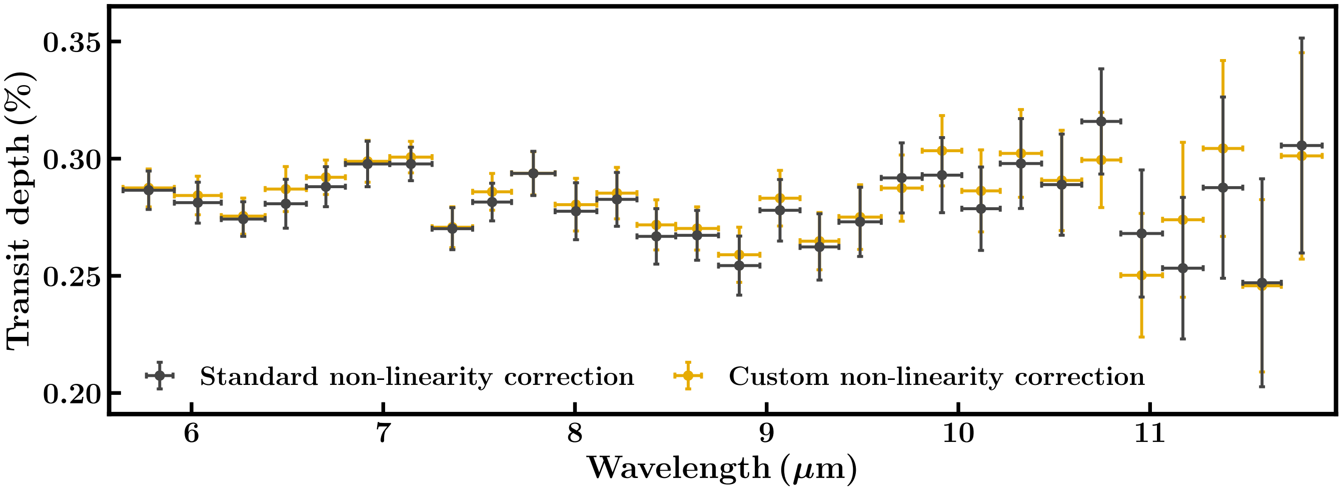

Figure 7. Effects of different nonlinearity corrections on the MIRI transmission spectrum of K2-18 b. The spectra with the standard and our custom nonlinearity corrections are shown in dark gray and yellow, respectively.

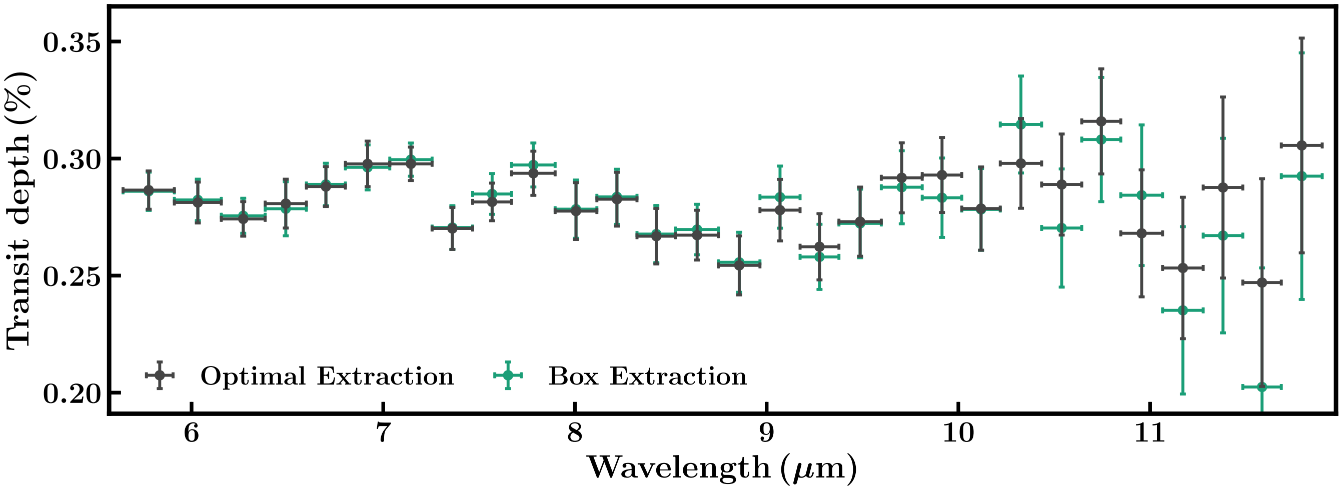

Figure 8. Comparisons between different spectral extraction methods. The dark gray points show the MIRI transmission spectrum of K2-18 b using the optimal extraction method, while the green points show the spectrum using box extraction.

A.4. Spectral Binning

Previous work has shown that transmission spectra obtained with MIRI LRS can be excessively noisy when using small spectroscopic bins (T. J. Bell et al. 2024). Therefore, recent works have adopted wide bins with typical widths of 0.15–0.5 μm (e.g., T. J. Bell et al. 2024; D. Powell et al. 2024; E. Schlawin et al. 2024; L. Welbanks et al. 2024). In this work, we test the sensitivity of our transmission spectrum of K2-18 b to different bin sizes, as shown in Figure 9. We adopt four different bin widths: a maximum of 4 pixels or 0.2 μm (whichever contains the most pixels), a maximum of 5 pixels or 0.2 μm, 0.4 μm, and 0.8 μm. We limit the bin widths to at least 4 or 5 pixels to average over potential systematic effects. Note that we only use whole pixel rows, to avoid introducing correlations between different spectral channels. We find that our transmission spectrum is generally consistent between the different bin widths, apart from a small region below around 5.6 μm. Specifically, in this region, the spectrum is not consistent between the 4 and 5 pixel bin widths, i.e., the green and gray data points in Figure 9. For this reason, we do not include the data below 5.6 μm in our atmospheric retrievals. Nominally, we select a maximum of 5 pixels or 0.2 μm as our canonical binning for both `JExoRES` and `JexoPipe`. We also conduct atmospheric retrievals with varying bin widths using our canonical model. We find consistent results between the retrievals with detection significances for DMS+DMDS between 3.2σ and 3.3σ across the different bin widths, as shown in Table 2.

A.5. Trends in Light-curve Fitting

MIRI time-series observations are affected by detector settling, in which there is an exponential-like ramp in the light curves at the beginning of the observation (J. Bouwman et al. 2023; T. P. Greene et al. 2023). This effect can be seen in the white-light curve of our observation, as shown in Figure 1. A common approach to treating this effect is to mask some number of integrations at the start of the observation and/or to account for the detector settling when fitting the light curves (e.g., J. Bouwman et al. 2023; D. Grant et al. 2023; T. P. Greene et al. 2023; E. M. R. Kempton et al. 2023; T. J. Bell et al. 2024; A. Dyrek et al. 2024)—for example, by including an exponential trend. For this reason, we investigate the impacts of different treatments of this effect on our MIRI transmission spectrum of K2-18 b. To model the light curves,

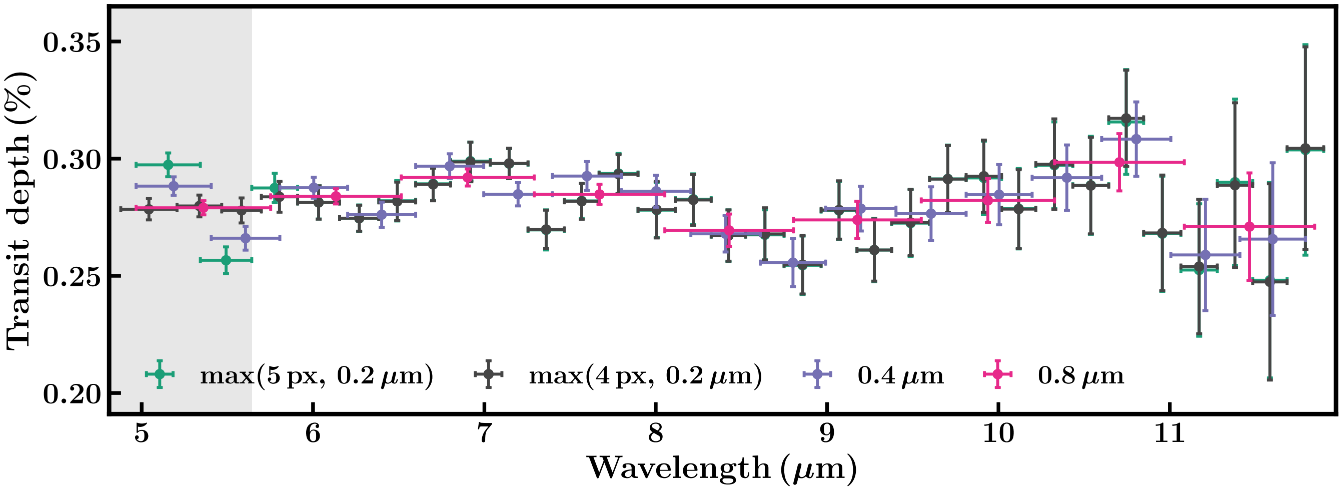

Figure 9. MIRI transmission spectrum of K2-18 b using different bin widths. For our analysis, we do not consider the spectrum below 5.6 μm to be conservative, given that the choice of binning affects the spectrum in this region. Note that these spectra did not use GPs, as discussed in Appendix A.7, thus the error bars may be somewhat underestimated.

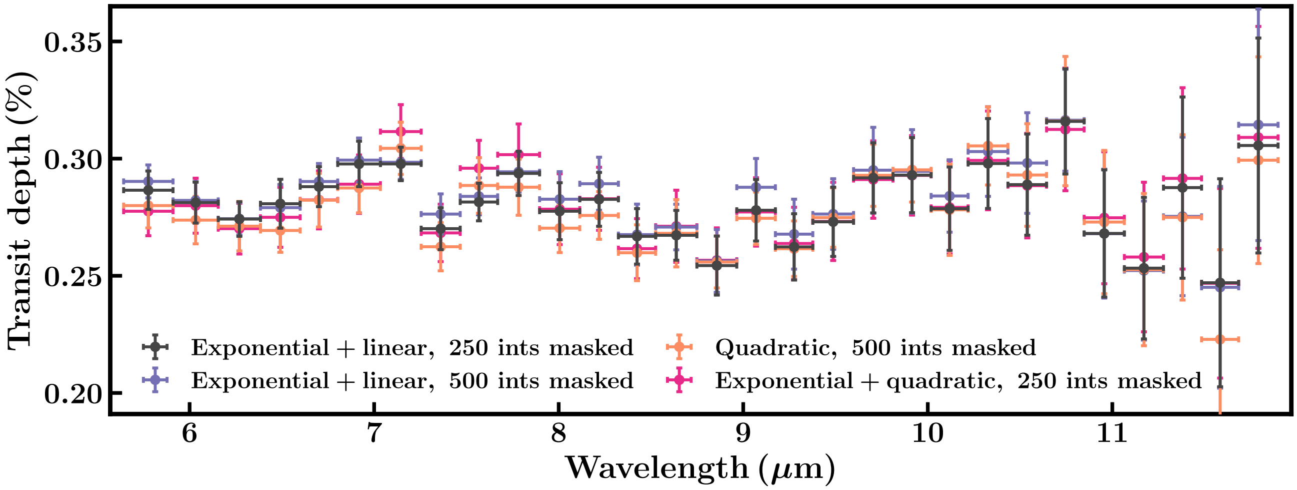

Figure 10. The MIRI transmission spectrum of K2-18 b obtained using different treatments of the detector settling effect. We consider an exponential + a linear trend (dark gray and purple), an exponential + a quadratic trend (pink), and a quadratic trend alone (orange), as well as different numbers of integrations to mask at the start of the observation.

we use the following systematic model:

$$F_{obs}(t) = F_{\text{out}}\,(1 + \alpha\tau + \beta\tau^2 + \gamma e^{-\tau/\epsilon})\,F_{\text{transit}}(t)\,, \qquad \text{(A4)}$$

where τ is the time since the start of the observation, F_{transit} is the `batman` transit model, and F_{out}, α, β, γ, and ϵ are trend parameters. We consider three different trend prescriptions: an exponential and a linear trend ($\beta = 0$, as described in Section 2.1), an exponential and a quadratic trend, and a quadratic trend alone ($\gamma = 0$). Note that for the white-light curve, we obtain a good fit to the data using the first option. Furthermore, we nominally remove 250 integrations (17 minutes) at the start of the observation, to remove the worst part of the detector settling effect. However, for the quadratic trend, we mask 500 integrations (34 minutes) at the start, to remove even more of the settling effect. Figure 10 shows the MIRI transmission spectrum of K2-18 b obtained using different trends, showing general agreement between these scenarios. For our canonical case with an exponential and a linear trend, we also consider a wider range of the number of masked integrations, between 125 and 750 integrations, and find that the spectrum is consistent across these cases (as shown in Figure 10 for 250 and 500 masked integrations).

A.6. Limb Darkening

In our canonical data reduction, for both `JExoRES` and `JexoPipe`, we fix the quadratic limb-darkening coefficients to the values estimated from the corresponding white-light curves, as given in Table 1. This is motivated by the small and approximately wavelength-independent limb darkening in the mid-infrared, between 5 and 12 μm. To test this assumption, we generate a transmission spectrum of K2-18 b using wavelength-dependent model limb-darkening coefficients obtained via ExoCTK (M. Bourque et al. 2021). For this, we use an ATLAS9 model (F. Castelli & R. L. Kurucz 2003)—predicting $u_1 = 0.028 \pm 0.008$ and $u_2 = 0.107 \pm 0.011$ when integrating over the MIRI LRS bandpass (5–10 μm)—in agreement with our white-light-curve estimates. Figure 11 shows that the transmission spectrum of K2-18 b does not significantly differ between our two approaches, highlighting

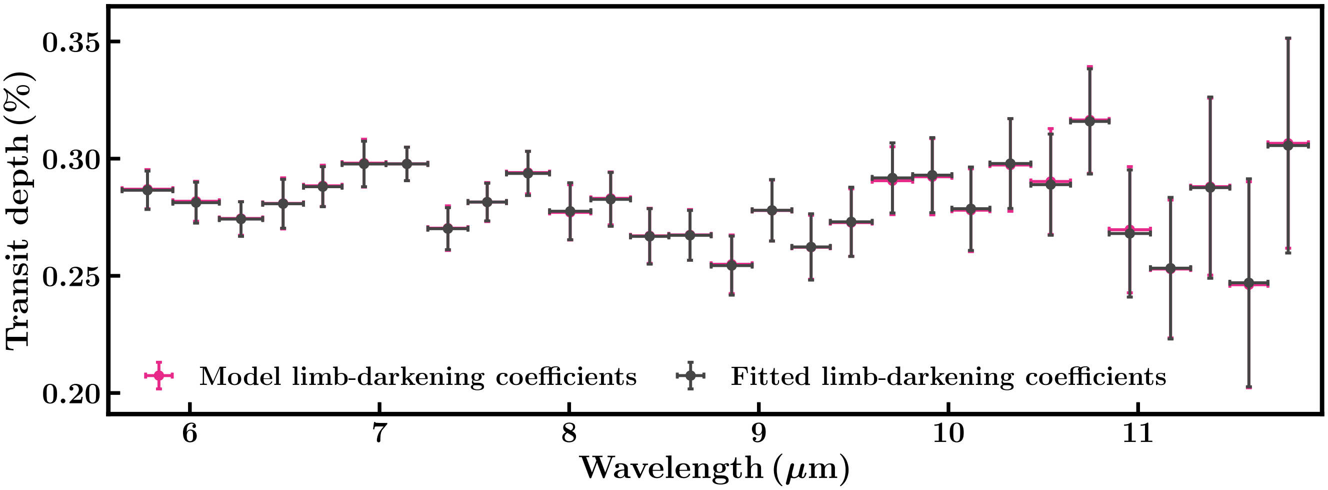

Figure 11. Comparison of different limb-darkening assumptions on the MIRI transmission spectrum of K2-18 b. The wavelength-dependent model limb-darkening case is shown in pink, while the wavelength-independent empirical limb-darkening case is shown in dark gray. The model limb-darkening coefficients were obtained using an ATLAS9 model (F. Castelli & R. L. Kurucz 2003), computed via ExoCTK (M. Bourque et al. 2021).

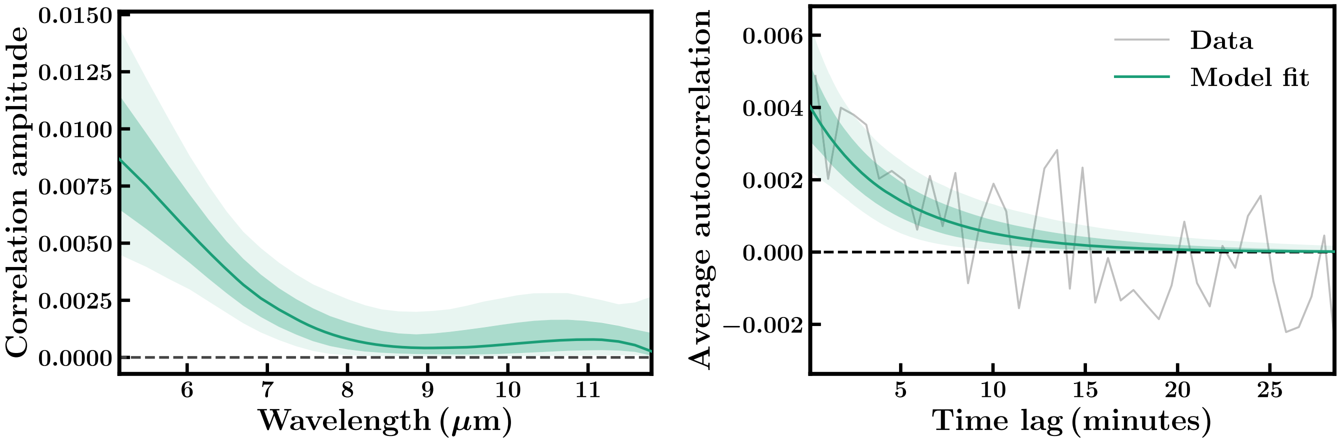

Figure 12. Illustration of the correlation amplitude ρ (left) and the average autocorrelation function (right). The median fit is shown in solid green, while the 1σ and 2σ regions are shown in two lighter shades of green.

the robustness of the spectrum with respect to the effect of limb darkening.

A.7. Time-correlated Noise

We find evidence for time-correlated noise when analyzing the light curves. By inspecting the autocorrelation functions as a function of wavelength, we find that the time-correlated noise has a timescale of a few minutes and that the amplitude of this noise increases toward shorter wavelengths. To account for this, we fit a model of the noise to the residuals of the light curves after subtracting the fitted transit models and while masking the first hour of the observation. Based on the exponential-like shape of the autocorrelation functions, we employ the following wavelength-dependent GP kernel:

$$\kappa_\lambda(t_i, t_j) = \sigma_\lambda^2\, \delta_{ij} + \rho(\lambda)\, \sigma_\lambda^2\, e^{-|t_i - t_j|/\eta}\,, \tag{A5}$$

where σ_λ is the standard deviation of a spectral channel with central wavelength λ, $\rho(\lambda)$ is a smooth function describing the amplitude of the time-correlated noise, and η is the timescale of this noise (assumed to be wavelength-independent). We parameterize $\rho(\lambda)$ as a cubic polynomial, defined by four points that are equally spaced in wavelength. This gives us five parameters in total to describe the kernel. To estimate these parameters, we add up the log-likelihoods from each spectral channel, as computed via `celerite` (D. Foreman-Mackey et al. 2017), and use `MultiNest` (F. Feroz et al. 2009) to obtain the posterior distributions. Figure 12 shows the estimated $\rho(\lambda)$ together with the average autocorrelation function.

Next, we use the median $\rho(\lambda)$ and η to refit the light curves with the above kernel, again using `celerite` to evaluate the likelihood. For this, we do not use an error inflation parameter, as that is already taken into account by σ_λ. We find that the center points of the spectrum (that is, the median values of the transit depth posterior distributions) remain very similar to the case without using the kernel (Equation (A5)), while the transit depth uncertainties increase by around 0%–30%, reaching a maximum at the shortest wavelengths. Figure 13 shows the transit depth uncertainties with and without our GP model. Given these findings, we use the GP case as our canonical `JExoRES` spectrum, which has more conservative error bars.

As an additional robustness check, we also account for time-correlated noise using a different method in the `JexoPipe` pipeline, applying the "time-averaging" method (J. N. Winn et al. 2007; P. Cubillos et al. 2017). Here, we obtain Allan deviation

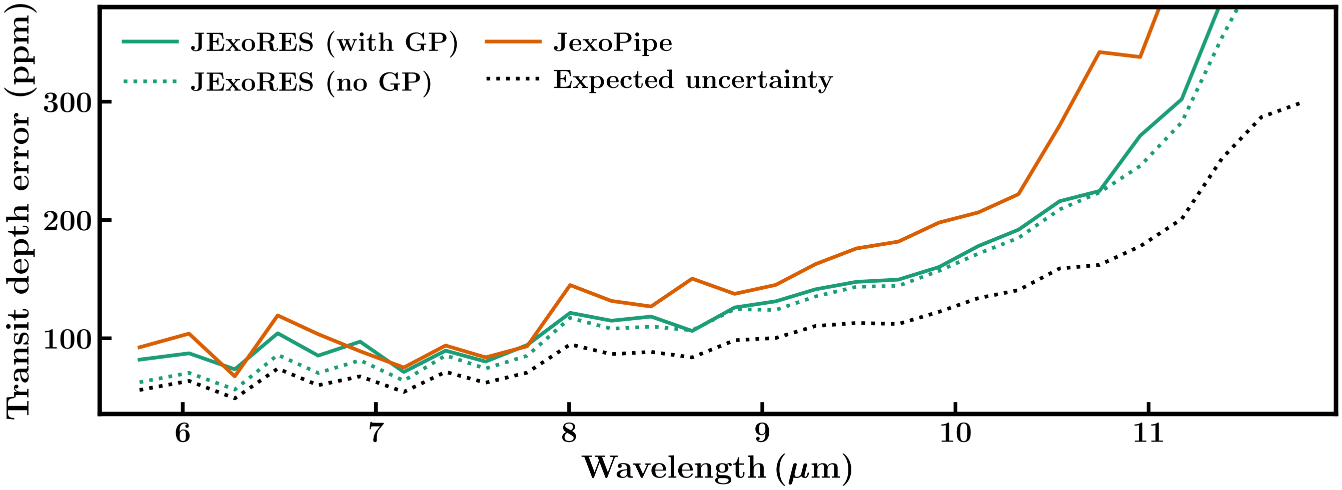

Figure 13. Transit depth uncertainties of our MIRI transmission spectrum of K2-18 b with 0.2 μm bins. The solid and dotted green lines show the uncertainties for `JExoRES`, with and without using the GP model, respectively, as discussed in Appendix A.7. The solid orange line shows the uncertainties obtained with `JexoPipe`, as also discussed in Appendix A.7. The dotted line shows the expected uncertainties, obtained by propagating the photon and read noise.

plots for the residuals from each spectral light curve and find the average β factor for bins between 5 and 20 minutes duration, where β is the ratio between the observed fractional noise and the expected value for uncorrelated noise. Including only β values $\geqslant 1$, we find a median β of 1.14 across all the spectral bins used. To account for correlated noise, we then inflate the errors on the light-curve data points by these factors and repeat the light-curve fits. This gives the final `JexoPipe` spectrum used for retrieval analysis with conservative error bars. Figure 13 shows the final transit depth uncertainties.

Appendix B
Retrieval Setup

The present retrievals consider atmospheric opacity contributions from several molecular species. As discussed in Section 3.1, for the maximal retrieval, we consider opacity contributions from 20 notable molecular species. We compute the absorption cross sections from line list data, following S. Gandhi & N. Madhusudhan (2017) and S. Gandhi et al. (2020), for CH_4 (S. N. Yurchenko & J. Tennyson 2014), CO_2 (S. A. Tashkun et al. 2015), H_2O (R. J. Barber et al. 2006; L. S. Rothman et al. 2010), NH_3 (S. N. Yurchenko et al. 2011), CO (G. Li et al. 2015), SO_2 (D. S. Underwood et al. 2016), HCN (R. J. Barber et al. 2014), H_2S (A. A. A. Azzam et al. 2016; K. L. Chubb et al. 2018), CH_3OH (J. J. Harrison et al. 2012), C_2H_2 (L. Gomez et al. 2010; I. E. Gordon et al. 2022), C_2H_4 (J. V. Auwera et al. 2007; I. E. Gordon et al. 2022), C_2H_6 (Z. D. Reed & J. T. Hodges 2015), CH_3Cl (C. Bray et al. 2011; A. Nikitin et al. 2016), OCS (J.-P. Bouanich et al. 1986; L. Régalia-Jarlot et al. 2002; H. Müller et al. 2005; J. V. Auwera & A. Fayt 2006; K. Sung et al. 2009; R. Toth et al. 2010; D. Golebiowski et al. 2014), N_2O (L. Daumont et al. 2001), and PH_3 (I. E. Gordon et al. 2022). For DMS, DMDS, CH_3SH, and CS_2, we consider the HITRAN (S. W. Sharpe et al. 2004; I. Gordon et al. 2017; R. Kochanov et al. 2019) absorption cross sections at 1 bar and 298 K, similar to N. Madhusudhan et al. (2021). Table 3 shows the priors and retrieved constraints for all free parameters of the canonical model and the models without DMDS or DMS.

Figure 14 shows spectral contributions from a number of the molecules listed above with significant cross sections in the mid-infrared, which are included in the maximal atmospheric model described in Section 3.1. Figure 15 shows the posterior distributions retrieved for 10 of the 20 molecular species considered in the maximal atmospheric model. Only one of the 20 molecules, DMDS, is well constrained by the data for this retrieval. Figure 16 shows the posteriors for all the parameters for the canonical retrieval discussed in Sections 3.1 and 3.2, also showing a peak in the posterior for DMDS. When DMDS is removed from the model a peak in the posterior is found for DMS, as shown in Figure 5.

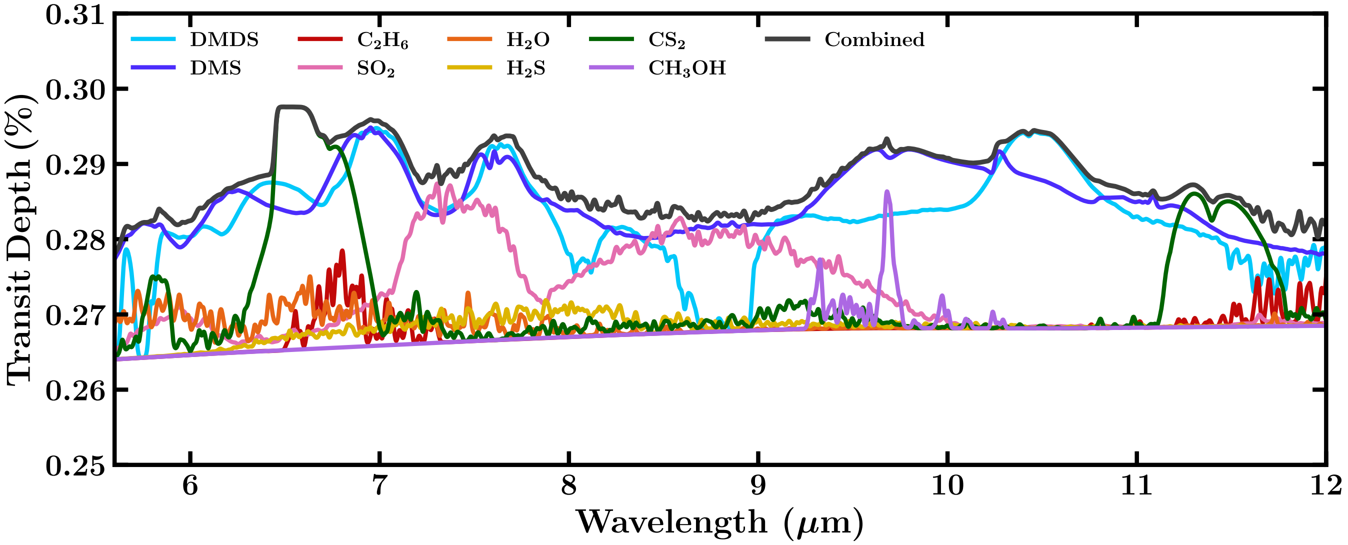

Figure 14. Spectral contributions from DMDS and DMS, also shown in Figure 4, as well as several other molecular species with significant cross sections in the mid-infrared considered in the maximal retrieval described in Section 3.1. All mixing ratios are set to 5×10^{-4}.

Table 3
Retrieved Atmospheric Parameters and Corresponding Prior Probability Distributions for the Canonical Retrieval with the `JExoRES` Spectrum

Parameter	Bayesian Prior	Description	DMS + DMDS	DMS Only	DMDS Only
$\log(X_{\rm DMDS})$	$\mathcal{U}(-12, -0.3)$	Mixing ratio of DMDS	$-3.48^{+1.24}_{-2.27}$	…	$-3.25^{+1.17}_{-1.30}$
$\log(X_{\rm DMS})$	$\mathcal{U}$(-12, -0.3)	Mixing ratio of DMS	$-6.35^{+2.75}_{-3.47}$	$-3.42^{+1.16}_{-1.44}$	…
$\log(X_{\rm CH_4})$	$\mathcal{U}(-12, -0.3)$	Mixing ratio of CH_4	$-6.66^{+3.22}_{-3.22}$	$-6.89^{+3.23}_{-3.25}$	$-6.82^{+3.23}_{-3.17}$
$\log(X_{\rm CO_2})$	$\mathcal{U}(-12, -0.3)$	Mixing ratio of CO_2	$-6.42^{+2.75}_{-3.47}$	$-6.72^{+3.53}_{-3.34}$	$-6.59^{+3.40}_{-3.35}$
T_0/K	$\mathcal{U}(100, 500)$	Temperature at 0.1 μbar	354^{+129}_{-126}	370^{+131}_{-145}	344^{+128}_{-131}
$T_{\rm 1mbar}$/K	…	Temperature at 1 mbar	422^{+141}_{-133}	438^{+145}_{-157}	402^{+143}_{-129}
α_1/K$^{-\frac{1}{2}}$	$\mathcal{U}(0.02, 2.00)$	*P–T* profile curvature	$1.16^{+0.50}_{-0.50}$	$1.19^{+0.50}_{-0.53}$	$1.20^{+0.50}_{-0.50}$
α_2/K$^{-\frac{1}{2}}$	$\mathcal{U}(0.02, 2.00)$	*P–T* profile curvature	$1.12^{+0.58}_{-0.54}$	$1.12^{+0.55}_{-0.60}$	$1.11^{+0.59}_{-0.55}$
$\log(P_1$/bar)	$\mathcal{U}(-6, 1)$	*P–T* profile region limit	$-2.53^{+1.11}_{-1.25}$	$-2.53^{+1.10}_{-1.24}$	$-2.43^{+1.08}_{-1.28}$
$\log(P_2$/bar)	$\mathcal{U}(-6, 1)$	*P–T* profile region limit	$-4.45^{+1.28}_{-0.98}$	$-4.50^{+1.27}_{-0.98}$	$-4.40^{+1.33}_{-1.03}$
$\log(P_3$/bar)	$\mathcal{U}(-2, 1)$	*P–T* profile region limit	$-0.84^{+0.53}_{-0.65}$	$-0.88^{+0.58}_{-0.67}$	$-0.84^{+0.54}_{-0.63}$
$\log(P_{\rm ref}$/bar)	$\mathcal{U}(-6, 0)$	Reference pressure at $R_{\rm P}$	$-4.32^{+1.15}_{-0.93}$	$-4.27^{+1.30}_{-0.96}$	$-4.22^{+1.27}_{-1.03}$
$\log(a)$	$\mathcal{U}(-4, 10)$	Rayleigh enhancement factor	$2.23^{+3.92}_{-4.49}$	$2.51^{+4.46}_{-4.01}$	$2.94^{+4.34}_{-4.36}$
γ	$\mathcal{U}(-20, 2)$	Scattering slope	$-9.51^{+6.42}_{-6.42}$	$-10.01^{+6.49}_{-6.35}$	$-9.93^{+6.63}_{-6.43}$
$\log(P_{\rm c}$/bar)	$\mathcal{U}(-6, 1)$	Cloud-top pressure	$-2.20^{+1.92}_{-1.96}$	$-1.90^{+1.86}_{-2.02}$	$-2.21^{+1.87}_{-1.94}$
ϕ	$\mathcal{U}(0, 1)$	Cloud/haze coverage fraction	$0.49^{+0.31}_{-0.30}$	$0.45^{+0.32}_{-0.30}$	$0.46^{+0.31}_{-0.29}$
$\delta_{\rm MIRI}$/ppm	$\mathcal{U}(-100, 100)$	MIRI data set offset	-12^{+51}_{-58}	22^{+48}_{-63}	-12^{+52}_{-61}

Note. The quoted parameter values denote the retrieved median and 1σ intervals. The $T_{\rm 1mbar}$ values are inferred from the retrieved *P–T* profile parameter constraints.

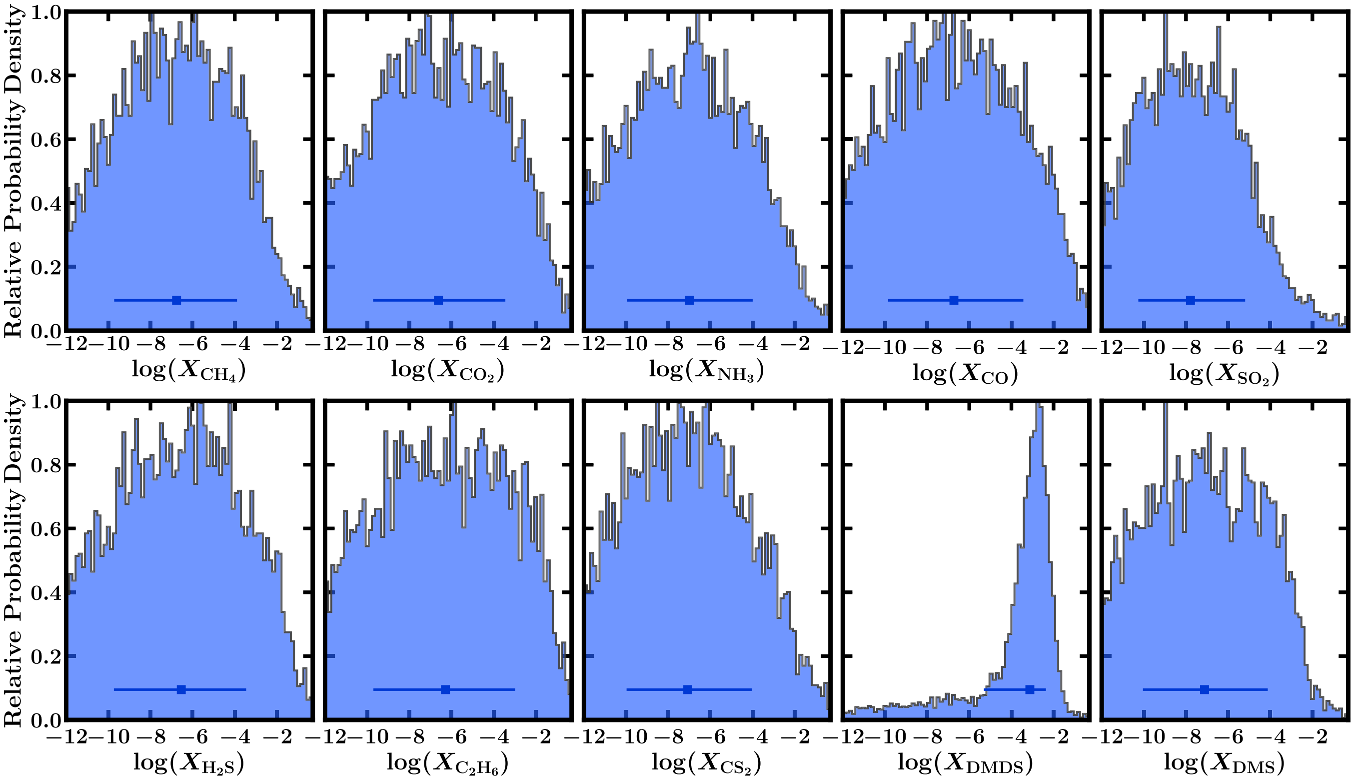

Figure 15. Posterior probability distributions of mixing ratios for a number of molecular species included in the maximal retrieval described in Section 3.1. We find that only one out of the 20 species considered, DMDS, has a well-constrained posterior, as shown. When DMDS is removed from the model, a peak in the posterior is found for DMS.

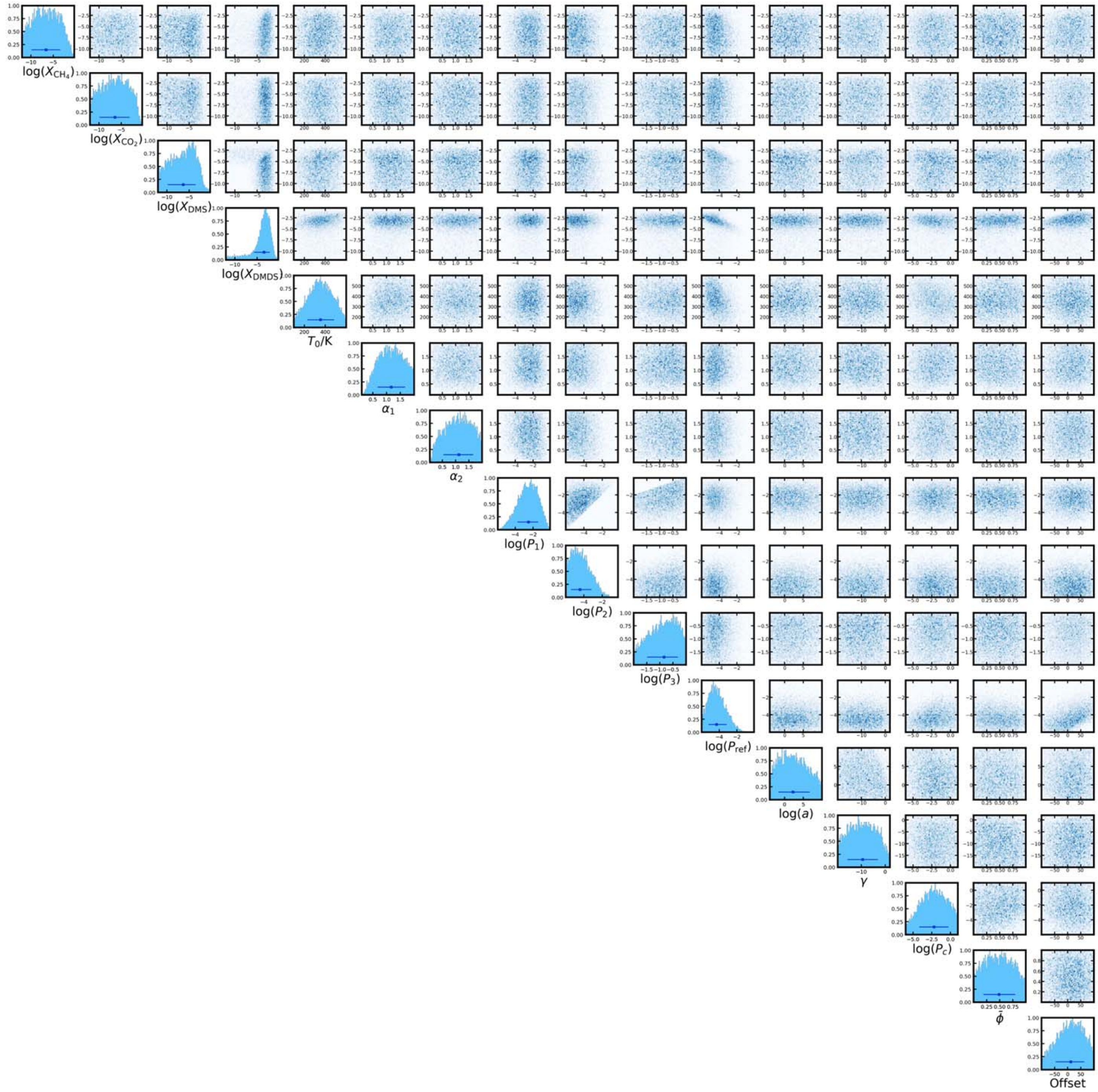

Figure 16. Posterior probability distribution for the canonical retrieval using the `JExoRES` spectrum. The diagonal panels show the posterior probability distribution for each parameter and the off-diagonal panels show the pairwise correlations. The horizontal error bars denote the median and 1σ intervals for each parameter.

ORCID iDs

Nikku Madhusudhan https://orcid.org/0000-0002-4869-000X
Savvas Constantinou https://orcid.org/0000-0001-6839-4569
Måns Holmberg https://orcid.org/0000-0002-0931-735X
Subhajit Sarkar https://orcid.org/0000-0002-2705-5402
Anjali A. A. Piette https://orcid.org/0000-0002-4487-5533
Julianne I. Moses https://orcid.org/0000-0002-8837-0035

References

Abel, M., Frommhold, L., Li, X., & Hunt, K. L. C. 2011, JPCA, 115, 6805
Alam, M. K., Gao, P., Adams Redai, J., et al. 2025, AJ, 169, 15
Alderson, L., Batalha, N. E., Wakeford, H. R., et al. 2024, AJ, 167, 216
Auwera, J. V., & Fayt, A. 2006, JMoSt, 780, 134
Auwera, J. V., Moazzen-Ahmadi, N., & Flaud, J.-M. 2007, ApJ, 662, 750
Azzam, A. A. A., Tennyson, J., Yurchenko, S. N., & Naumenko, O. V. 2016, MNRAS, 460, 4063
Barber, R. J., Strange, J. K., Hill, C., et al. 2014, MNRAS, 437, 1828
Barber, R. J., Tennyson, J., Harris, G. J., & Tolchenov, R. N. 2006, MNRAS, 368, 1087
Barclay, T., Kostov, V. B., Colón, K. D., et al. 2021, AJ, 162, 300
Bell, T. J., Crouzet, N., Cubillos, P. E., et al. 2024, NatAs, 8, 879
Benneke, B., Roy, P.-A., Coulombe, L.-P., et al. 2024, arXiv:2403.03325
Benneke, B., Wong, I., Piaulet, C., et al. 2019, ApJL, 887, L14
Bézard, B., Charnay, B., & Blain, D. 2022, NatAs, 6, 537
Bieler, A., Altwegg, K., Balsiger, H., et al. 2015, Natur, 526, 678

Blain, D., Charnay, B., & Bézard, B. 2021, A&A, 646, A15

Borysow, J., Frommhold, L., & Birnbaum, G. 1988, ApJ, 326, 509

Bouanich, J.-P., Blanquet, G., Walrand, J., & Courtoy, C. P. 1986, JQSRT, 36, 295

Bourque, M., Espinoza, N., Filippazzo, J., et al. 2021, The Exoplanet Characterization Toolkit (ExoCTK), v1.0.0, Zenodo, doi:10.5281/zenodo.4556063

Bouwman, J., Kendrew, S., Greene, T. P., et al. 2023, PASP, 135, 038002

Bray, C., Perrin, A., Jacquemart, D., & Lacome, N. 2011, JQSRT, 112, 2446

Buchner, J. 2021, JOSS, 6, 3001

Buchner, J., Georgakakis, A., Nandra, K., et al. 2014, A&A, 564, A125

Bushouse, H. 2020, in ASP Conf. Ser. 527, Astronomical Data Analysis Software and Systems XXIX, ed. R. Pizzo et al. (San Francisco, CA: ASP), 583

Castelli, F., & Kurucz, R. L. 2003, in IAU Symp. 210, Modelling of Stellar Atmospheres, ed. N. Piskunov, W. W. Weiss, & D. F. Gray (San Francisco, CA: ASP), A20

Catling, D. C., Krissansen-Totton, J., Kiang, N. Y., et al. 2018, AsBio, 18, 709

Chubb, K. L., Naumenko, O., Keely, S., et al. 2018, JQSRT, 218, 178

Cloutier, R., Astudillo-Defru, N., Doyon, R., et al. 2017, A&A, 608, A35

Cloutier, R., Astudillo-Defru, N., Doyon, R., et al. 2019, A&A, 621, A49

Constantinou, S., & Madhusudhan, N. 2024, MNRAS, 530, 3252

Constantinou, S., Madhusudhan, N., & Gandhi, S. 2023, ApJL, 943, L10

Cooke, G. J., & Madhusudhan, N. 2024, ApJ, 977, 209

Court, R. W., & Sephton, M. A. 2012, P&SS, 73, 233

Cubillos, P., Harrington, J., Loredo, T. J., et al. 2017, AJ, 153, 3

Damiano, M., Bello-Arufe, A., Yang, J., & Hu, R. 2024, ApJL, 968, L22

Daumont, L., Auwera, J., Teffo, J.-L., Perevalov, V., & Tashkun, S. 2001, JMoSp, 208, 281

Domagal-Goldman, S. D., Meadows, V. S., Claire, M. W., & Kasting, J. F. 2011, AsBio, 11, 419

Dyrek, A., Min, M., Decin, L., et al. 2024, Natur, 625, 51

Fayolle, E. C., Öberg, K. I., Jørgensen, J. K., et al. 2017, NatAs, 1, 703

Felton, R. C., Bastelberger, S. T., Mandt, K. E., et al. 2022, JGRE, 127, e06853

Feroz, F., Hobson, M. P., & Bridges, M. 2009, MNRAS, 398, 1601

Foreman-Mackey, D., Agol, E., Ambikasaran, S., & Angus, R. 2017, AJ, 154, 220

Foreman-Mackey, D., Hogg, D. W., Lang, D., & Goodman, J. 2013, PASP, 125, 306

Fukui, A., Kimura, T., Hirano, T., et al. 2022, PASJ, 74, L1

Gandhi, S., Brogi, M., Yurchenko, S. N., et al. 2020, MNRAS, 495, 224

Gandhi, S., & Madhusudhan, N. 2017, MNRAS, 472, 2334

Gardner, J. P., Mather, J. C., Clampin, M., et al. 2006, SSRv, 123, 485

Glein, C. R. 2024, ApJL, 964, L19

Golebiowski, D., de Ghellinck d'Elseghem Vaernewijck, X., Herman, M., Vander Auwera, J., & Fayt, A. 2014, JQSRT, 149, 184

Gomez, L., Jacquemart, D., Lacome, N., & Mandin, J.-Y. 2010, JQSRT, 111, 2256

Gordon, I., Rothman, L., Hill, C., et al. 2017, JQSRT, 203, 3-69

Gordon, I. E., Rothman, L. S., Hargreaves, R. J., et al. 2022, JQSRT, 277, 107949

Grant, D., Lewis, N. K., Wakeford, H. R., et al. 2023, ApJL, 956, L32

Grant, D., & Wakeford, H. R. 2024, JOSS, 9, 6816

Greene, T. P., Bell, T. J., Ducrot, E., et al. 2023, Natur, 618, 39

Hänni, N., Altwegg, K., Combi, M., et al. 2024, ApJ, 976, 74

Harrison, J. J., Allen, N. D. C., & Bernath, P. F. 2012, JQSRT, 113, 2189

He, C., Hörst, S. M., Lewis, N. K., et al. 2020, NatAs, 4, 986

Holmberg, M., & Madhusudhan, N. 2023, MNRAS, 524, 377

Holmberg, M., & Madhusudhan, N. 2024, A&A, 683, L2

Horne, K. 1986, PASP, 98, 609

Hu, R. 2021, ApJ, 921, 27

Innes, H., Tsai, S.-M., & Pierrehumbert, R. T. 2023, ApJ, 953, 168

Kawauchi, K., Murgas, F., Palle, E., et al. 2022, A&A, 666, A4

Kempton, E. M. R., Zhang, M., Bean, J. L., et al. 2023, Natur, 620, 67

Kendrew, S., Scheithauer, S., Bouchet, P., et al. 2015, PASP, 127, 623

Khare, B. N., Sagan, C., Bandurski, E. L., & Nagy, B. 1978, Sci, 199, 1199

Kipping, D. M. 2013, MNRAS, 435, 2152

Kochanov, R., Gordon, I., Rothman, L., et al. 2019, JQSRT,

Kreidberg, L. 2015, PASP, 127, 1161

Krissansen-Totton, J., Olson, S., & Catling, D. C. 2018, SciA, 4, eaao5747

Leconte, J., Spiga, A., Clément, N., et al. 2024, A&A, 686, A131

Leung, M., Schwieterman, E. W., Parenteau, M. N., & Fauchez, T. J. 2022, ApJ, 938, 6

Li, G., Gordon, I. E., Rothman, L. S., et al. 2015, ApJS, 216, 15

Lim, O., Benneke, B., Doyon, R., et al. 2023, ApJL, 955, L22

Luu, C. N., Yu, X., Glein, C. R., et al. 2024, ApJL, 977, L51

Madhusudhan, N., Moses, J. I., Rigby, F., & Barrier, E. 2023a, FaDi, 245, 80

Madhusudhan, N., Nixon, M. C., Welbanks, L., Piette, A. A. A., & Booth, R. A. 2020, ApJL, 891, L7

Madhusudhan, N., Piette, A. A. A., & Constantinou, S. 2021, ApJ, 918, 1

Madhusudhan, N., Sarkar, S., Constantinou, S., et al. 2023b, ApJL, 956, L13

Madhusudhan, N., & Seager, S. 2009, ApJ, 707, 24

May, E. M., MacDonald, R. J., Bennett, K. A., et al. 2023, ApJL, 959, L9

Meadows, V., Graham, H., Abrahamsson, V., et al. 2022, arXiv:2210.14293

Mikal-Evans, T., Madhusudhan, N., Dittmann, J., et al. 2023, AJ, 165, 84

Montet, B. T., Morton, T. D., Foreman-Mackey, D., et al. 2015, ApJ, 809, 25

Moran, S. E., Stevenson, K. B., Sing, D. K., et al. 2023, ApJL, 948, L11

Morrison, J. E., Dicken, D., Argyriou, I., et al. 2023, PASP, 135, 075004

Müller, H., Schlöder, F., Stutzki, J., & Winnewisser, G. 2005, JMoSt, 742, 215

Nikitin, A., Dmitrieva, T., & Gordon, I. 2016, JQSRT, 177, 49

Orton, G. S., Gustafsson, M., Burgdorf, M., & Meadows, V. 2007, Icar, 189, 544

Piaulet, C., Benneke, B., Almenara, J., et al. 2023, NatAs, 7, 206

Pierrehumbert, R. T. 2023, ApJ, 944, 20

Piette, A. A. A., & Madhusudhan, N. 2020, ApJ, 904, 154

Pinhas, A., Madhusudhan, N., Gandhi, S., & MacDonald, R. 2019, MNRAS, 482, 1485

Powell, D., Feinstein, A. D., Lee, E. K. H., et al. 2024, Natur, 626, 979

Raulin, F., & Toupance, G. 1975, OrLi, 6, 91

Reed, N. W., Shearer, R. L., McGlynn, S. E., et al. 2024, ApJL, 973, L38

Reed, Z. D., & Hodges, J. T. 2015, JQSRT, 159, 87

Régalia-Jarlot, L., Hamdouni, A., Thomas, X., der Heyden, P. V., & Barbe, A. 2002, JQSRT, 74, 455

Richard, C., Gordon, I. E., Rothman, L. S., et al. 2012, JQSRT, 113, 1276

Rigby, F. E., Pica-Ciamarra, L., Holmberg, M., et al. 2024, ApJ, 975, 101

Rothman, L. S., Gordon, I. E., Barber, R. J., et al. 2010, JQSRT, 111, 2139

Rubin, M., Altwegg, K., Balsiger, H., et al. 2019, MNRAS, 489, 594

Sagan, C., & Khare, B. N. 1971, ApJ, 168, 563

Sarkar, S., Madhusudhan, N., Constantinou, S., & Holmberg, M. 2024, MNRAS, 531, 2731

Sarkis, P., Henning, T., Kürster, M., et al. 2018, AJ, 155, 257

Scarsdale, N., Wogan, N., Wakeford, H. R., et al. 2024, AJ, 168, 276

Scheucher, M., Wunderlich, F., Grenfell, J. L., et al. 2020, ApJ, 898, 44

Schlawin, E., Mukherjee, S., Ohno, K., et al. 2024, AJ, 168, 104

Schwieterman, E. W., Kiang, N. Y., Parenteau, M. N., et al. 2018, AsBio, 18, 663

Schwieterman, E. W., & Leung, M. 2024, RvMG, 90, 465

Seager, S., Bains, W., & Hu, R. 2013a, ApJ, 775, 104

Seager, S., Bains, W., & Hu, R. 2013b, ApJ, 777, 95

Segura, A., Kasting, J. F., Meadows, V., et al. 2005, AsBio, 5, 706

Sharpe, S. W., Johnson, T. J., Sams, R. L., et al. 2004, ApSpe, 58, 1452

Shorttle, O., Jordan, S., Nicholls, H., Lichtenberg, T., & Bower, D. J. 2024, ApJL, 962, L8

Skilling, J. 2004, in AIP Conf. Ser. 735, Bayesian Inference and Maximum Entropy Methods in Science and Engineering: 24th International Workshop on Bayesian Inference and Maximum Entropy Methods in Science and Engineering, ed. R. Fischer, R. Preuss, & U. V. Toussaint (Melville, NY: AIP), 395

Sousa-Silva, C., Seager, S., Ranjan, S., et al. 2020, AsBio, 20, 235

Sung, K., Toth, R., Brown, L., & Crawford, T. 2009, JQSRT, 110, 2082

Tashkun, S. A., Perevalov, V. I., Gamache, R. R., & Lamouroux, J. 2015, JQSRT, 152, 45

Toth, R., Sung, K., Brown, L., & Crawford, T. 2010, JQSRT, 111, 1193

Tsai, S.-M., Innes, H., Lichtenberg, T., et al. 2021, ApJL, 922, L27

Tsai, S.-M., Innes, H., Wogan, N. F., & Schwieterman, E. W. 2024, ApJL, 966, L24

Tsiaras, A., Waldmann, I. P., Rocchetto, M., et al., 2016 pylightcurve: Exoplanet lightcurve model, Astrophysics Source Code Library, ascl:1612.018

Tsiaras, A., Waldmann, I. P., Tinetti, G., Tennyson, J., & Yurchenko, S. N. 2019, NatAs, 3, 1086

Underwood, D. S., Tennyson, J., Yurchenko, S. N., et al. 2016, MNRAS, 459, 3890

Vehtari, A., Gelman, A., & Gabry, J. 2017, Statistics and computing, 27, 1413

VonNiederhausern, D. M., Wilson, G. M., & Giles, N. F. 2006, JCED, 51, 1990

Vuitton, V., Moran, S. E., He, C., et al. 2021, PSJ, 2, 2

Wallack, N. L., Batalha, N. E., Alderson, L., et al. 2024, AJ, 168, 77

Welbanks, L., Bell, T. J., Beatty, T. G., et al. 2024, Natur, 630, 836

Welbanks, L., McGill, P., Line, M., & Madhusudhan, N. 2023, AJ, 165, 112

Winn, J. N., Holman, M. J., Bakos, G. Á., et al. 2007, AJ, 134, 1707

Wogan, N. F., Batalha, N. E., Zahnle, K. J., et al. 2024, ApJL, 963, L7

Yang, J., & Hu, R. 2024, ApJL, 971, L48

Yu, X., Moses, J. I., Fortney, J. J., & Zhang, X. 2021, ApJ, 914, 38

Yurchenko, S. N., Barber, R. J., & Tennyson, J. 2011, MNRAS, 413, 1828

Yurchenko, S. N., & Tennyson, J. 2014, MNRAS, 440, 1649

Zahnle, K. 1996, in IAU Colloq. 156: The Collision of Comet Shoemaker-Levy 9 and Jupiter, ed. K. S. Noll, H. A. Weaver, & P. D. Feldman (Cambridge: Cambridge Univ. Press), 183